NUCLEAR REACTIONS -- EXPERIMENTAL

USING RADIOACTIVE BEAMS TO PROBE HEAVY-ION REACTION MECHANISMS

S.J.Yennello, B. Young, J. Yee, J. Winger, G.D. Westfall, A. Vander Molen, B. Sherrill, D.J. Morrissey, T. Li, E. Gualtieri, W. Benenson, D. Bazin, E. Norbeck[a] and J. Shea[b]

The combination of the K1200 cyclotron, the A1200 fragment analyzer and the 4π Array at Michigan State University has allowed the first study of nuclear fragmentation reaction mechanisms induced by a radioactive beam.

The use of heavy-ion beams to study fragmentation mechanisms permits the degrees of freedom of mass and asymmetry of the system to be investigated. The development of the A1200 fragment analyzer at the MSU/NSCL now allows an additional degree of freedom, N/Z, to be investigated. The placement of the A1200, directly at the exit of the K1200 cyclotron, enables the secondary beams to then be transported to experimental stations throughout the laboratory. The use of the MSU 4π array is well suited to the limited beam currents available from secondary beams because of its large solid angle coverage.

In order to detect isotopically resolved intermediate mass fragments, 13 silicon detector telescopes were positioned at 11.3°, 39° and 141° within the 4π Array. Complete event characterization was obtained by detection of nearly all light charged particles and intermediate mass fragments in the 4π bragg curve and phoswich detectors. The reactions of 53 Mev/A ^{40}Ca, ^{40}Ar, ^{40}Cl beams with ^{58}Ni and ^{58}Fe targets were used to investigate the effects of changing N/Z within a constant mass system. Fragment yields and energy spectra will be examined as a function of N/Z of the system.

A system of PPACs and silicon PIN diodes was used to identify the ^{40}Cl at the focal plane and verify transmission of the correct isotope to the 4π and determine it's purity. A beam intensity of 1.9×10^{6} pps of 90+% pure ^{40}Cl was focused on the target of the 4π.

a. University of Iowa

b. University of Maryland

THE DISAPPEARANCE OF FLOW

G.D. Westfall, A.M. Vander Molen, J.S. Winfield, S.J. Yennello, T. Li, J. Yee, E. Gualtieri, S. Hannuschke, D. Craig, R. Lacey, A. Nadasen, M. Cronqvist, and E. Norbeck

One of the major goals of nucleus-nucleus collisions is to determine information about the nuclear equation of state (EOS). Great strides toward this goal were made by the Plastic Ball group[1] and the Streamer Chamber group[2] at the Bevalac. These groups found that collective flow increased with increasing mass of the system and with the incident energy. The systems studied included Ca+Ca, Nb+Nb, La+La, and Au+Au at energies ranging from 150 to 1000 MeV/nucleon. By comparing to various models they attempted to determine the incompressibility of nuclear matter, K. They found that a stiff EOS (K = 380 MeV) was needed to explain the experimental results.

More recently improvements to transport models such the Boltzmann-Uehling-Uelenbeck (BUU) model have cast doubt on the validity of the information extracted concerning the EOS. The inclusion of momentum dependent interactions and the possibility that the nucleon-nucleon cross sections, σ_{nn}, used in the BUU calculations could be modified by in-medium effects have a large effect on the predictions of the model. Thus we have proposed to extract information about the EOS by measuring the incident energy at which the nucleus-nucleus interaction which is dominantly attractive at energies around 10 MeV/nucleon changes over to the dominantly repulsive interaction observed at energies around 1000 MeV/nucleon. This energy is called the balance energy, E_{bal} [3].

The advantage of the observable E_{bal} is that the comparison of experimental observables to the BUU calculations is simplified. To compare the predictions of the BUU model directly to the experimental data is difficult because the BUU model makes predictions only for protons and neutrons. In the experiment many light nuclei are observed in addition to nucleons. Thus it is difficult to take the results of the BUU model and filter them through the acceptance of the experimental apparatus because the response of detectors depends on the type of fragment being measured. In addition, the magnitude of the observed flow has been shown to depend of the mass of the observed fragment. However, at a given incident energy corresponding to E_{bal}, flow will be predicted to be zero regardless of whether the model incoporates fragment formation. The predicted value for E_{bal} can be compared directly with the experimentally determined quantity and information about the EOS can be extracted.

The first observation of the disappearance of flow was made by Krofcheck et al. using the Lawrence Berkeley Laboratory streamer chamber at the Bevalac with the Michigan State University (MSU) charge coupled device (CCD) camera system where flow was observed to disappear at an incident energy of around 50 MeV/nucleon for La+La[4]. Ogilvie et al. next observed that flow disappeared in the system Ar+V around 85 MeV/nucleon[3] using the MSU 4π Array and the K1200 superconducting cyclotron. A similar measurement was made at GANIL by Sullivan et al.[5] for the system Ar+Al using the Mur/Tonneau where flow was also observed to disappear around 85 MeV/nucleon. An upper limit of around 50 MeV/nucleon for Au+Au was established by Zhang et al. using a time-of-flight wall at the LBL Bevalac[6].

However, the first determination of E_{bal} in which flow was observed to disappear and then reappear was made by Krofcheck et al. for the Ar+V system[7] at NSCL with the MSU 4π Array. In this measurement E_{bal} was determined to be 85 $\pm$ 10 MeV/nucleon. This result is illustrated in Fig. 1 where collective flow for Z=2 fragments from Ar+V reaction from 35 to 100 MeV/nucleon. One can clearly see flow return at

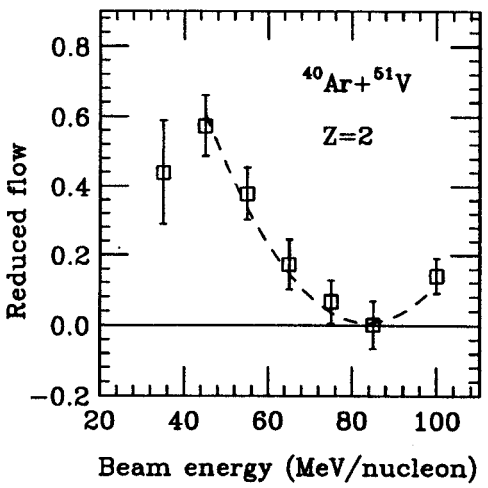

Figure 1: The disappearance of flow in the system Ar+V. The quantity plotted is the reduced flow for Z=2 fragments from central collisions.

incident energies above E_{bal} [7]. In the present work we will present two new measurements of E_{bal}. These measurements were carried with the MSU 4π Array with the Bragg curve counters (BCCs) installed. For the system Ar+Sc we find that E_{bal} is 89 $\pm$ 5 MeV/nucleon and for Kr+Nb we find 65 $\pm$ 5 MeV/nucleon.

The present work was carried out using the MSU 4π Array[8]. This device consisted of a main ball of phoswich counters composed of 170 fast/slow plastic scintillators arranged in 30 separate subarrays.

The fast plastic ΔE was 3 mm thick and the slow plastic E was 25 cm thick. The gains of the main ball phoswich counters were set to accept fragments with Z up to 6. A BCC was installed in front of each of the 30 subarrays of phoswich counters. The thickness of the gas was 15 cm. For the Ar+Sc measurements P5 gas (95% argon, 5% methane) at a pressure of 500 torr was used. For the Kr+Nb measurements a heavy freon (C_2F_6) was used with a pressure of 100 torr. The gains of the gas counters were set to accept fragments with Z up to 13. The entrance window was 900 $\mu g/cm^2$ kapton supported by a wire grid. The anodes of the forward five modules were subdivided to allow higher singles count rates. The gas counters were used in transmission mode with the fast plastic serving as the E counter. Particles that stopped in fast plastic were identified using the gas counter and the fast plastic scintillator while those that punched through the fast plastic and stopped in the slow plastic were identified using the fast and slow plastic scintillators.

We present here new results for the disappearance of flow for the systems Ar+Sc and Kr+Nb. Flow measurements were made at 35, 45, 65, 75, 85, 95, 105, and 115 MeV/nucleon for Ar+Sc and at 35, 45, 55, 60, 65, 70, and 75 MeV/nucleon for Kr+Nb.

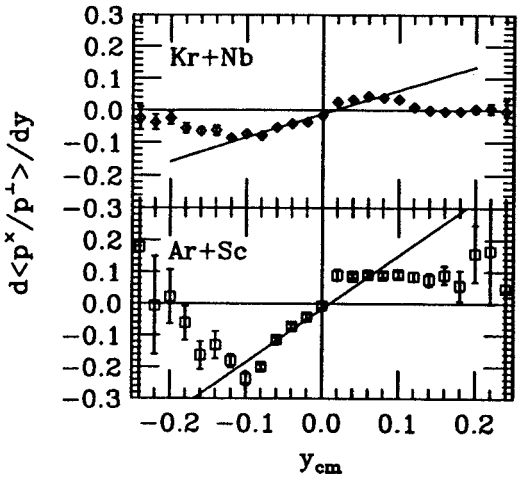

Figure 2: Average transverse momentum divided by the total transverse momentum as a function on center of mass rapidity for central collisions of 35 MeV/nucleon Ar+Sc and Kr+Nb.

The first step in the analysis of these data was to determine the centrality of the collisions. We used mid-rapidity charge (Z_{mr}) to determine the impact parameter[10]. Mid-rapidity charge is defined as all charge observed with center of mass rapidity, y_{cm}, greater than 75% of the target rapidity and less than 75%

of the projectile rapidity. Central events corresponding to about 10% of the total cross section were selected. The reaction plane was determined using the method of azimuthal correlations[9]. Auto-correlation effects were treated by removing the particle of interest from the reaction plane determination. The average transverse momentum in the reaction plane divided by the total transverse momentum, $< p^x/p^\perp >$, is then calculated as a function of y_{cm} for a given type of observed fragment. In Fig. 2 $< p^x/p^\perp >$ is shown as a function of y_{cm} for helium fragments from 35 MeV/nucleon Ar+Sc and Kr+Nb. Central collisions were selected in both cases. The typical S-shaped curve is observed with positive values of $< p^x/p^\perp >$ being observed for projectile-like rapidities and negative values begin observed for target-like rapidities. The reduced flow is defined as the slope of this curve, $d < p^x/p^\perp > /dy$, at mid-rapidity. The rapidity range over which the slope is determined is $0.8y_t \leq y_{cm} \leq 0.8y_p$ where $y_t(y_p)$ is the target(projectile) rapidity in the center of mass.

The reduced flow is plotted in Fig. 3 as a function of the incident energy for the systems for tritons

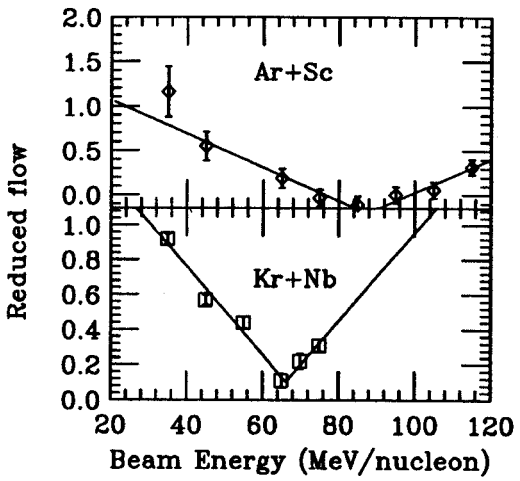

Figure 3: Reduced flow as a function of incident energy for central collisions of a) t from Ar+Sc and b) He from Kr+Nb.

from Ar+Sc and helium fragments from Kr+Nb. Other fragments show results of similar or better quality. The solid line corresponds to a fit under the assumption that the observed reduced flow decreases linearly with increasing beam energy, reaches a zero which corresponds to E_{bal}, and then begins to increase linearly again. The absolute magnitude of the slope of both lines is taken to be the same. For the system Ar+Sc we find that E_{bal} is 89 $\pm$ 5 MeV/nucleon and for Kr+Nb we find 65 $\pm$ 5 MeV/nucleon.

The BUU model incorporates effects concerning the EOS through the mean field interaction as well as direct scattering of the constituent nucleons. In principle one can extract information concerning the EOS by comparing experimental observables to the results of the BUU calculations. The comparison of the predicted E_{bal} to the measured value has several advantages including a lack of sensitivity to any imprecision in the determination of the reaction plane and a lack of sensitivity to fragment production.

Here we present BUU calculations carried out by Bauer and Gale from Ref. 11. These calculations include momentum dependent interactions. The calculations are carried out for the system Nb+Nb, which is similar to Kr+Nb, at an impact parameter of 2 fm. The sensitivity to the parameters of the EOS is show in Fig. 4a where calculations for a hard EOS (K=380 MeV) and a soft EOS (K=200 MeV). The predicted

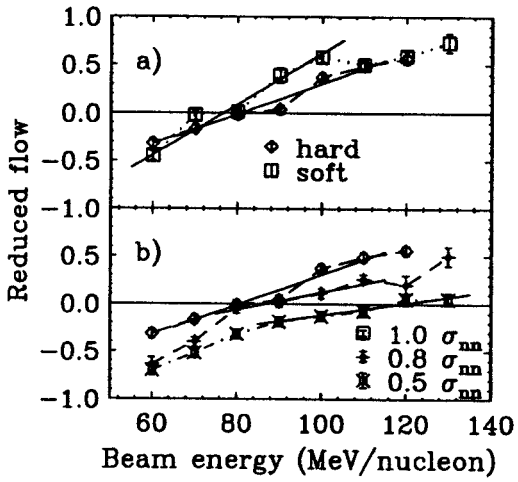

Figure 4: BUU calculations for central collisions of Nb+Nb. a) Hard (K=380 MeV) and soft (K=200 MeV) equation of state. b) Effect of lowering of scattering cross sections in BUU by factors of 1.0, 0.8, and 0.5 for a hard equation of state. Solid lines are least square fits around the zero crossing point.

E_{bal} changes from 76 to 81 MeV/nucleon. Thus the comparison of this result to the experimental result for Kr+Nb cannot yield information concerning the parameters of the EOS. In Fig. 4b the effect of lowering the nucleon-nucleon cross sections as might be expected from certain in-medium effects is demonstrated. Three calculations are shown in Fig. 4b for a hard EOS. The three calculations correspond to values of the free nucleon-nucleon cross sections scaled by factors of 1.0, 0.8, and 0.5. As the cross sections are lowered, the predicted E_{bal} changes from 81 to 87 to 119 MeV/nucleon. Clearly drastic reductions in the cross sections on the order of 50% are ruled out by the experimental results.

In conclusion we have presented two new sets of experimental results for the disappearance of flow, Ar+Sc and Kr+Nb. We observed that E_{bal} decreases from 89 to 65 MeV/nucleon as the mass of the system increases from Ar+Sc to Kr+Nb. Comparisons with the BUU rule out drastic reductions in the nucleon-nucleon cross sections in the nuclear medium. However, the extraction of detailed information concerning the EOS still awaits a complete, systematic set of data containing accurate E_{bal} measurements.

References

1. H.H. Gutbrod, A.M. Poskanzer, and H.G. Ritter, Rep. Prog. Phys. 52, 1267 (1989).
2. P. Danielewicz, H. Ströbele, G. Odyniec, D. Bangert, R. Bock, R. Brockmann, J.W. Harris, H.G. Pugh, W. Rauch, R.E. Renfordt, A. Sandoval, D. Schall, L.S. Schroeder and R. Stock, Phys. Rev. C 38, 120 (1988).
3. C.A. Ogilvie, W. Bauer, D.A. Cebra, J. Clayton, S. Howden, J. Karn, A. Nadasen, A. Vander Molen, G.D. Westfall, W.K. Wilson, and J.S. Winfield, Phys. Rev. C 42, R10 (1990).
4. D. Krofcheck, W. Bauer, G.M. Crawley, C. Djalali, S. Howden, C.A. Ogilvie, A. Vander Molen, G.D. Westfall, and W.K. Wilson, R.S. Tickle, and C. Gale, Phys. Rev. Lett. 63, 2028 (1989).
5. J.P. Sullivan, J Péter, D. Cussol, G. Bizard, R. Brou, M. Louvel, J.P. Patry, R. Regimbart, J.C. Steckmeyer, B. Tamain, E. Crema, H. Doubre, K. Hagel, G.M. Jin, A. Péghaire, F. Saint-Laurent, Y. Cassagnou, R. Lebrun, E. Rosato, R. Macgrath, S.C. Jeong, S.M. Lee, Y. Nagashima, T. Nakagawa, M. Ogihara, J. Kasagi, and T. Motobayashi, Phys. Lett. 249B, 8 (1990).
6. W.M. Zhang, R. Madey, M. Elaasar, J. Schambach, D. Keane, B.D. Anderson, A.R. Baldwin, J. Cogar, J.W. Watson, G.D. Westfall, G. Krebs, and H. Wieman, Phys. Rev. C 42, R491 (1990).
7. D. Krofcheck, D.A. Cebra, M. Cronqvist, R. Lacey, T. Li, C.A. Ogilvie, A. Vander Molen, K. Tyson, G.D. Westfall, W.K. Wilson, J.S. Winfield, A. Nadasen, and E. Norbeck, Phys. Rev. C 43, 350 (1991).
8. G.D. Westfall, J.E. Yurkon, J. van der Plicht, Z.M. Koenig, B.V. Jacak, R.Fox, G.M. Crawley, M.R. Maier, B.E. Hasselquist, R.S. Tickle, and D. Horn, Nucl. Inst. Meth. 238, 347 (1985).
9. W.K. Wilson, R. Lacey, C.A. Ogilvie, and G.D. Westfall, Phys. Rev. C 45, 768 (1992).
10. C.A. Ogilvie, D.A. Cebra, J. Clayton, S. Howden, J. Karn, A. Vander Molen, G.D. Westfall, W.K. Wilson, and J.S. Winfield, Phys. Rev. C 40, 654 (1989).
11. D. Krofcheck, W. Bauer, G.M. Crawley, S. Howden, C.A. Ogilvie, A. Vander Molen, G.D. Westfall, W.K. Wilson, R.S. Tickle, C. Djalali, and C. Gale, submitted to Phys. Rev. C, MSUCL-815 (1992).

SUBTHRESHOLD PION PRODUCTION FROM CHARACTERIZED EVENTS

S.Hannuschke, A.Vander Molen, G.D.Westfall, E.Gualtieri, T.Lee,
B.Llope, A.Nadasen[a], E.Norbeck[b], J.Winfield, J.Yee, and S.Yennello

The study of subthreshold pion production can provide information about the formation of hot nuclear matter in intermediate energy nucleus- nucleus collisions and lead to understanding of the nuclear equation of state (EOS).[1,2] Because pions must be created in the reaction rather than be merely liberated, they are dominantly emitted from the hottest and most dense regions created in central collisions. Pions have been observed from collisions with incident energies as low as 25 MeV/nucleon.[1] The production of pions can be understood in terms of the BUU model except at the very lowest incident energies where an abnormally high momentum tail of the Fermi distribution of the constituent nucleons has to be assumed to explain the observed data.

A great deal of work has been done in understanding the inclusive production of pions from a variety of systems. In general, the production cross sections and energy spectra can be understood in terms of BUU.[2] One striking feature that has emerged recently is the small variation in the slope parameter, T_0, of the pion invariant cross section spectra at 90° in the center of mass frame for beam energies below 100 MeV/nucleon.[1]

Pion production has been studied from characterized events at Saclay at high energies (400, 600, 800 MeV/nucleon) using Diogene.[3] Pion flow was observed to be positive for all rapidities. This positive flow was attributed to absorption of the pions in nuclear matter. At intermediate energies pion production has been studied using the MUR at GANIL in coincidence with a single pion detector. The system studied was 94 MeV/nucleon O+Al.[4] The authors found that coincident particle distributions are very similar for high energy protons and pions and are very different than those from inclusive reactions. In a similar experiment, pion production in coincidence with fission fragments was studied using the system 95 MeV/nucleon O+Th. These authors concluded that pion production requires a large overlap of the target and projectile nuclei.

We propose to study pion production using the MSU 4π Array. The system we plan to study is Ne+Mg from 50 to 150 MeV/nucleon. The 4π Array should provide very high efficiency for the detection of π^+ and should provide a set of completely characterized events including impact parameter, reaction plane, degree of multifragmentation, and collective flow. The energies we are proposing cover the region

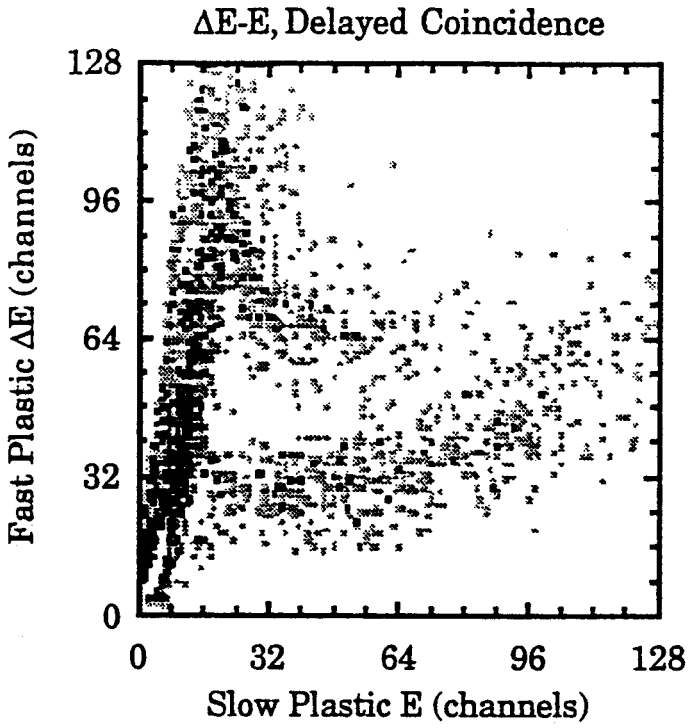

Figure 1: ΔE-E plot for particles satisfying the delayed coincidence requirement. The data are from 155 MeV/nucleon C+C. The pions are in the horizontal line in the middle of the figure.

where the liquid-gas phase transition may occur and lead to increased absorption of pions which is termed critical pion opacity.[6]

In addition we would like to search for any effect on the pion yields at the onset of multifragmentation. It is possible that the dynamics leading to these types of multiparticle final states may influence the production of pions. We also plan to study the flow of pions both in-plane and out-of-plane. These results should greatly enhance our knowledge of hot nuclear systems, especially the reabsorbtion coefficient for π^+ in nuclear matter.

We also plan to attempt to reproduce the surprising result that T_0 seems to change little from 25 to 100 MeV/nucleon.

Recently we demonstrated that we can detect pions using the 4π Array. We detected π^+ in a manner similar to that used by the Plastic Ball group.[7] We tagged the stopped pions with a delayed coincidence observing the $\mu^+ \rightarrow e^+ + \nu + \nu$ decay which has a mean life of 2.2 μs. The decay of the π^+ to μ^+ has a mean life of 26 nsec which is too short to be observed using the slow plastic of the ball phoswich

counters. To observe the μ^+ decay, we used a separate bank of FERAs for the E signal to record the pulseheight and time of the decay. Using this signal as a filter, we suppressed other particles and made the pions easy to identify in the ΔE-E spectra. In Figure 1 the ΔE-E plot for particles satisfying the delayed coincidence requirement is shown. This plot is the sum of three counters spanning the angles from 90 to 120 degrees for reactions of 155 MeV/nucleon C+C. The pion line is clear as well as protons that were randomly in coincidence with the delayed gate. In Figure 2 the time spectrum of the delayed coincidence

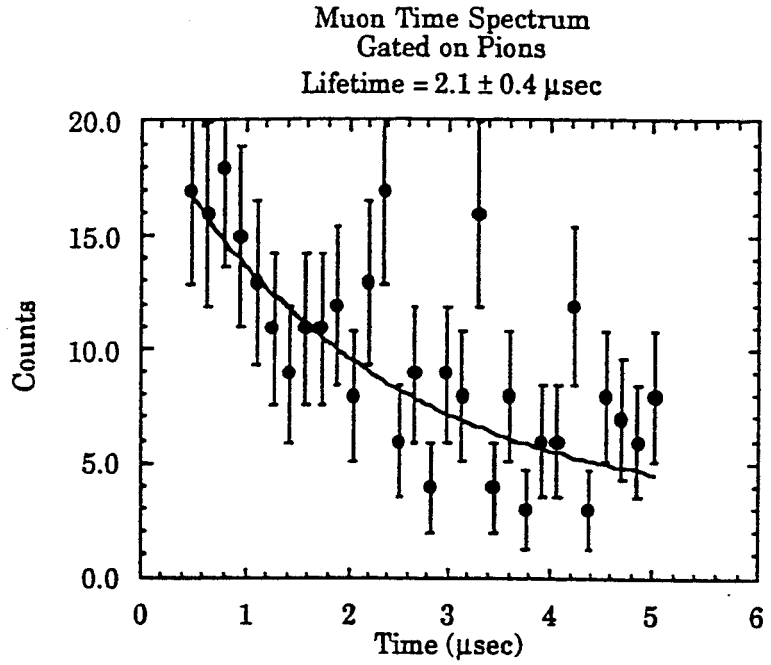

Figure 2: Time spectra for delayed coincidence gated on pions in the ΔE-E spectra. A constant background of three counts is assumed. The error bars are statistical.

in these counters is shown. Subtracting a fixed background of three counts, a mean life of $2.1 \pm 0.4 \mu$secs is observed which is in good agreement with the known mean life of the pion.

Currently we are investigating the response of the 4π phoswich counters to the $\mu^+ \rightarrow e^+ + \nu + \nu$ decay with respect to the range as well as the energy of the positron. Calculations are under way to determine the efficiency of the phoswich counters considering the range and differential energy loss of the positron and the response of adjacent modules. Comparisons of the calculated efficiency with data from a test with a pion beam are being considered.

a. University of Iowa

b. University of Michigan, Dearborn

References

1. T. Suziki, Proceedings of the 4th International Conference on Nucleus-Nucleus Collisions, Kanazawa, Japan, 1991, and references therein.
2. W. Bauer and B. Li, Proceedings of the Workshop on Relativistic Aspects of Nuclear Physics, 1991, World Scientific, and references therein.
3. J. Gosset et. al., Phys. Rev. Lett. 62, 1251 (1989).
4. A. Aiello et. al., EuroPhys. Lett. 6 (1), 25 (1988).
5. B. Erazmus et. al., Nucl. Phys. A481, 821 (1988).
6. W. Bauer, Preprint MSUCL-734, 1991.
7. H. Gutbrod et. al., NIM 203, 189 (1982).

SUBTHRESHOLD PION PRODUCTION AS A FUNCTION OF SYSTEM MASS

W. Benenson, D. Cebra, M. Cronqvist, P. Kirk[a], G. Krebs[b], J. Miller[b], T. Murakami[c], J.Panetta[b], R. Pfaff, T. Reposeur, L.S. Schroeder[b], J. Stevenson, T. Suzuki[d], I. Tanihata[d], A. Vandermolen, Z.-F. Wang[a], G.D. Westfall, J.S. Winfield, B. Young

To resolve a puzzle[1] in the mass dependence of subthreshold pion production we have measured the yield of π^- at 90° in the center of mass for Au + Au, La + La, and Ne +NaF collisions at E/A = 183 and 236 MeV. The experiment was carried out at the Lawrence Berkeley Laboratory Bevalac. The puzzle was that below threshold (E/A = 290 MeV) the cross section scaled much more rapidly with mass than expected from geometric considerations. The dependence was determined, however, by a comparison of data taken by several different groups (but with the same

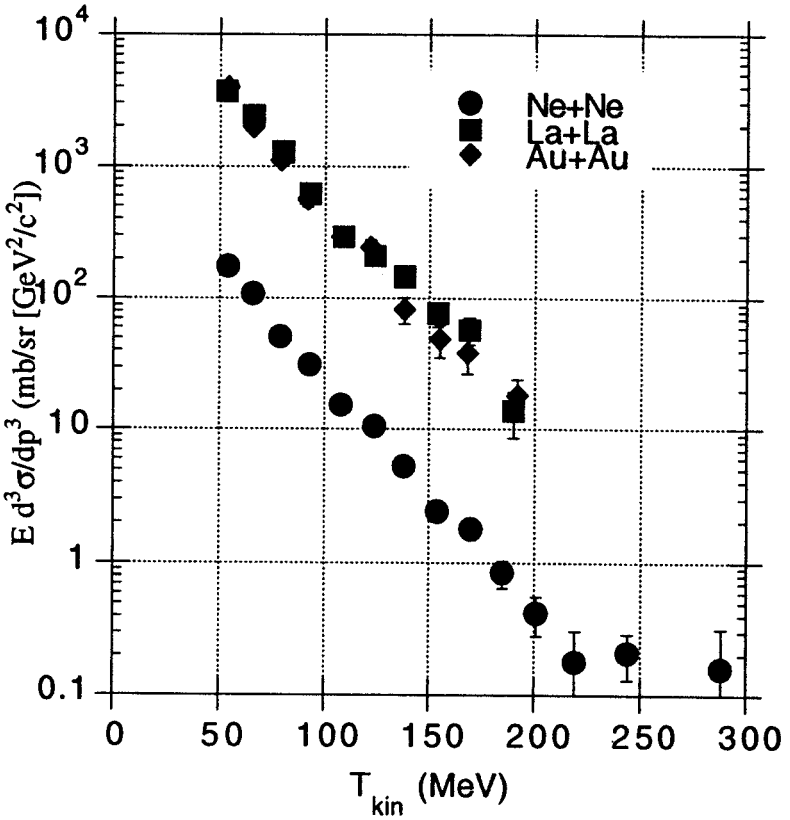

Fig 1. π^- Production at E/A = 183 MeV and Θ_{cm}=90°

spectrometer). In the present experiment, systematic errors were minimized by keeping the spectrometer fixed in angle and field and only varying the incident particle, beam energy and target.

The invariant cross section is given for the three systems in Fig. 1 as a function of pion kinetic energy for the lower beam energy. As can be seen, the shape is independent of system mass at E/A = 183 MeV. The E/A = 236 MeV data look very similar and have the same scaling with system mass. In fact the scaling between the light and heavy targets is very close to the $A^{1.7}$ which is normal for heavy ion reactions in this energy range. The smallness of difference between the La and Au data is not a significant violation of the normal scaling laws. The main difference between the present data and that presented in ref. 1 is in the Ne + NaF data, which is almost a factor of five larger in the present data as compared to the original[2] 1981 results..

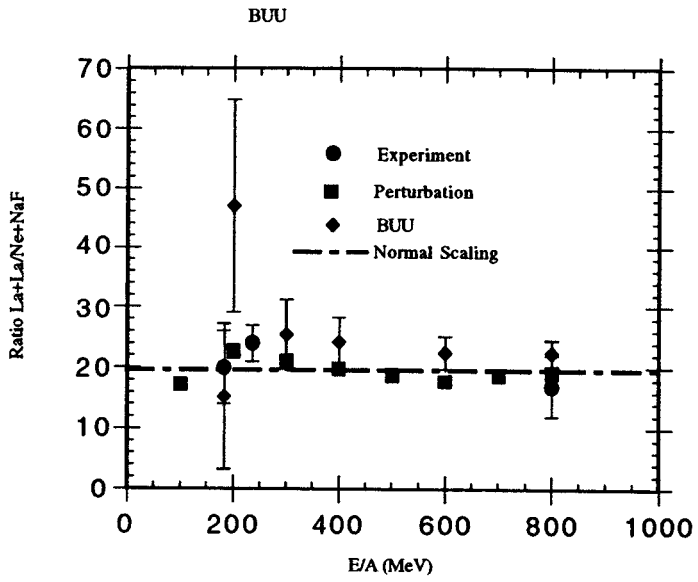

Fig 2 The ratio of the La+La cross section to that of Ne+ NaF as a function of beam energy. The two theoretical models, VUU and Perturbation are described in the text.

Comparison of the present work to two types of BUU calculations[3] by Li and Bauer give excellent agreement as is shown in Fig 2. The present data and the BUU calculations show clearly that the cross section for pion production scales with system mass in the manner expected from previous results in heavy ion collisions in this energy range and that there is no anomalous

enhancement of the yield for high mass systems. In Fig 2. the BUU calculation shows large statistical fluctuations because of the low probability of producing pions in these collisions, but the calculation is able to follow the pions interacting inside the nucleus after they are produced. On the other hand in the perturbation calculation the fractional probability of producing pions in each collisions is summed, and the absorption is treated in an approximate manner. Details of the scaling and the angular, multiplicity, and beam energy dependence of the pion cross section will aid in tying down the details of model representations.

[a] Louisiana State University
[b] Lawrence Berkeley Laboratory
[c] Tokyo Institute of Technology
[d] RIKEN, Japan

References

[1]J. Miller et al., Phys. Rev. Lett. **58**, 2408 (1987)
[2]S. Nagamiya et al. Phys. Rev. **C24**, 971(1981)
[3]B. A. Li and W. Bauer, to be published

REACTION PLANE DETERMINATION FOR $^{36}Ar + ^{197}Au$

M.B. Tsang, D.R. Bowman, N. Carlin,[a] C.K. Gelbke, Y.D. Kim[b], W.G. Lynch, L. Phair, R.T. de Souza,[b] and F. Zhu

In studies of intermediate-energy nucleus-nucleus collisions, many promising observables such as the collective flow [1], triple differential cross sections [2], are influenced strongly by the impact parameter and the orientation of the reaction plane. At low energies where fission fragments are detected, the plane spanned by the two coincident fission fragments has been used successfully as a handle for the reaction plane [3,4]. With increasing bombarding energies, fission process becomes less important and the reaction mechanism is dominated by emission of light charge particles and intermediate msss fragments. A method incorporating global information from all the detected particles to determine the reaction plane [5,6] is desirable. As charged particles are deflected to negative angles by the attractive nuclear mean field and they are emitted preferentially in the entrance channel reaction plane, the plane spanned by the beam axis and the major axis of the transverse momentum tensor of the emitted particles is the most logical choice for the reaction plane. To compare the accuracy with which the orientation of the reaction plane can be determined from the distribution of emitted light particles or coincident fission fragments, we have studied the azimuthal distributions for $^{36}Ar + ^{197}Au$ reactions at E/A=35 MeV with the NSCL 4π Miniball array [7]. Most experimental details had been given in ref [6,8,9] and will not be repeated here.

Fission fragments plane

Fission fragments that stop in the fast plastic scintillators were identified by the measured pulse height in the fast plastic and the corresponding time information. In addition, two fission particles must be detected in coincident in the miniball and must satisfy the condition $\Delta\phi_{ff} = 95^0\text{-}180^0$. The orientation of the fission plane is defined as

$$\Phi_F = .5*\{\phi_{f1}+\phi_{f2}+180^0\}\text{, modulo } 180^0 \qquad (1)$$

Azimuthal distributions of light particles and intermediate-mass fragments obtained with charge multiplicity gates from 4 to 9 are shown as open points in Fig. 1. Different panels of the figure show the azimuthal distribution of the indicated "trigger particle" with respect to the orientation of the fission plane. The distributions were normalized to an average value of unity. An energy gate of E/A = 12 - 20 MeV was applied to the trigger particles.

Transverse momentum tensor method

For each event with N-1 identified charged particles detected in coincidence with the trigger particle, we define the "reconstructed" reaction plane as the plane spanned by the beam axis and the major axis of the transverse momentum tensor for the N-1 coincident particles [6]. The azimuthal angle, Φ, of the reconstructed reaction plane then minimizes the sum,

$$\Sigma_p(\Phi) = \sum_{i=1}^{N-1} p_i^2 \sin^2\theta_i \sin^2(\phi_i - \Phi) . \qquad (2)$$

In Eq. 2, p_i, θ_i, and ϕ_i denote the momentum, polar and azimuthal angles of particle i in the laboratory system. (The beam axis defines $\theta=0^0$.) Azimuthal distributions of light particles and intermediate-mass fragments with respect to "reconstructed" reaction plane are shown as solid points in Fig. 1.

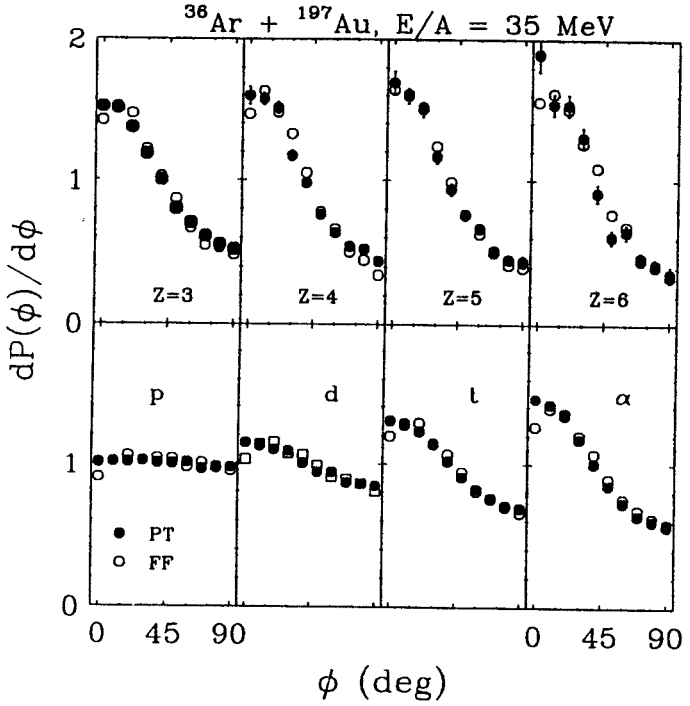

Figure 1: Azimuthal distributions of particles measured with respect to the fission plane, Eq. (1) (open points), and with respect to the plane determined from the major axis of the transverse momentum tensor, Eq. (2) (solid points). The elemental charge of the trigger particles, emitted at $\theta=45^0$, is indicated in the individual panels; the energy gates for the trigger particles were E/A=12-20 MeV.

Comparison between the two methods

Fig. 1 shows that quantitatively consistent azimuthal distributions are extracted from both methods, revealing enhanced emission in the reaction plane and the comparable accuracy of both methods

to determine the reaction for the $^{36}Ar + ^{197}Au$ reaction at E/A=35 MeV. It is important to know whether the two different techniques determine similar planes. Fig. 2 shows distributions $P(\Delta\Phi)$ of relative orientations between planes extracted from fission and tranverse momentum tensor. Since no polarizations are determined, the angle between any two planes can only be defined between $\Delta\Phi=0^0$ and 90^0. For convenience of comparison, we have adopted the normalization $P(\Delta\Phi=0^0)=1$. Relatively large differences exist between the orientation of the fission plane and the plane defined by the orientation of the major axis of the transverse momentum tensor constructed from the distribution of light particles and intermediate-mass fragments. These differences are shown by the solid points in Fig. 2. Nevertheless, the most probable relative orientation between the fission plane and planes extracted from the distribution of associated particles is $\Delta\Phi=0^0$. The rather broad distribution of $|\Phi_F-\Phi_{PT}|$ reflects limitations of the transverse momentum tensor and/or fission methods for average types of events. The distribution becomes narrower when one selects events with at least one energetic (E>80 MeV) alpha particle detected around 45^0, see open points in Fig. 2.

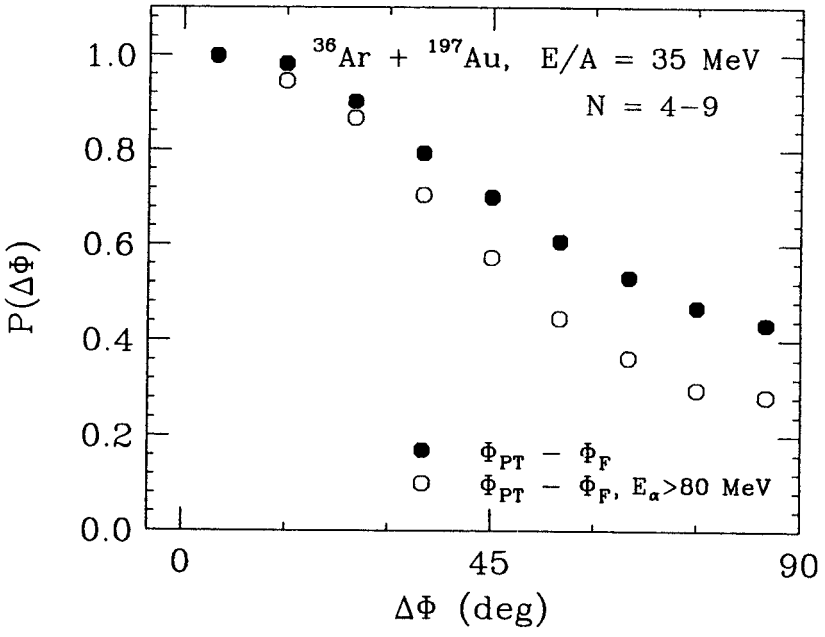

Figure 2: Distributions, $P(\Delta\Phi)$, of relative azimuthal orientations between planes determined by various methods. Φ_F is the azimuthal orientation of the fission plane, Eq. (1); Φ_{PT} denotes azimuthal orientations of the plane extracted from the detected charge particles distributions by means of Eqs 2. Solid and open points: $|\Phi_F - \Phi_{PT}|$ distributions for all events and for events with at least one energtic (E >80 MeV) α particle detected at $\theta=45^0$.

Estimate of experimental uncertainties

Experimental uncertainties of reaction plane reconstructions from transverse momentum tensor method can be estimated by randomly subdividing each event into two sub-events, each containing half

of the N-1 associated charged particles [10]. As an example, the left hand side of Fig. 3 shows "raw" azimuthal distributions, $P_r(\phi=|\phi_N - \Phi)$, relative to the reconstructed reaction plane for protons emitted at r=45° and selected by the multiplicity cut of N=9. The right hand side of Fig. 3 shows $P(\Phi_{12})$, the distribution of angles Φ_{12} between the two planes extracted (in analogy to Eq. 2) for the two sub-events detected in coincidents with the trigger particle. Under the assumption of statistical independence of sub-events, the distribution $P(\Phi_{12})$ is related to the distribution $P_{1/2}(\Phi)$ of relative orientations Φ between the true reaction plane and the planes reconstructed from the sub-events [6]:

$$P(\Phi_{12}) = \int P_{1/2}(\Phi)P_{1/2}(\Phi+\Phi_{12})d\Phi . \qquad (3)$$

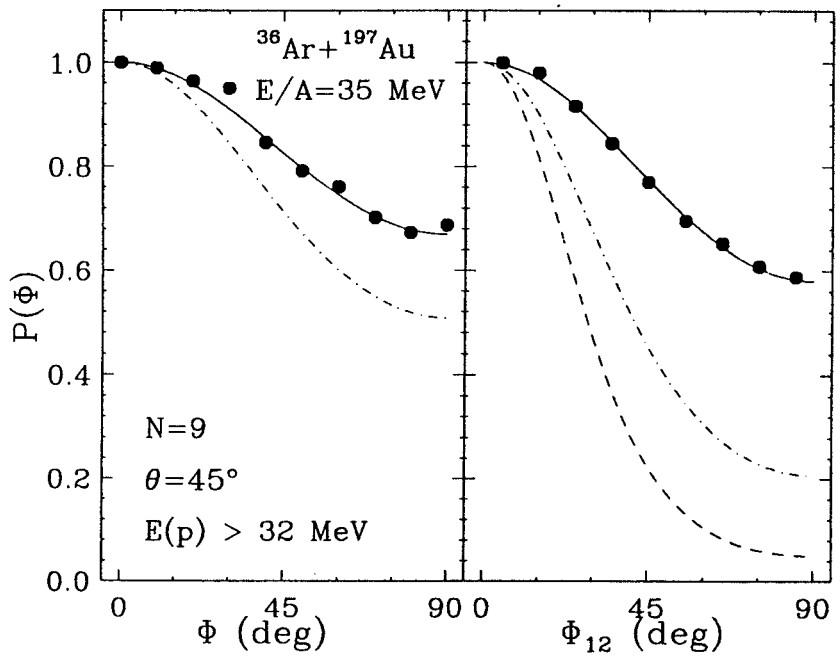

Figure 3: Left Hand panel: The points show azimuthal distributions, P (ϕ) of high energy protons (E_f> 32 MeV) relative to the reconstructed reaction plane. Right hand panel: The points show the measured distributions of the relative azimuthal angle, Φ_{12}, between planes determined by two sub-events of multiplicity (N-1)/2. See text for solid, dashed and dot-dashed curves.

The solid line in the right hand side of Fig. 3 shows the convolution obtained with the ansatz [6]

$$P_{1/2}(\Phi) = \exp(-\omega^2 \sin^2\Phi) , \qquad (4)$$

where ω is a fitting parameter. The function $P_{1/2}(\Phi)$ is depicted by the dot-dashed curve in the figure. The accuracy of reaction plane reconstruction is improved by using the full set of N-1 particles instead of the subset of (N-1)/2 particles. Monte-Carlo calculations [6] indicate that this

increase in accuracy may be readily assessed without sensitivity to detailed assumptions about the distribution of emitted particles. This improvement in accuracy is illustrated by the dashed curve in the right hand side of Fig. 3 which depicts $P(\Phi)$, the distribution of reaction planes reconstructed from the full set of N-1 associated particles.

For the emitted light particles, the raw azimuthal distributions $P_q(\phi)$ and the "true" distributions $P_t(\phi)$ with respect to the true reaction plane are related by the convolution

$$P_\gamma(\phi) = \int P_t(\Phi+\phi)P(\Phi)d\Phi \ . \qquad (5)$$

Good accuracy is achieved by approximating $P_t(\phi)$ and $P(\Phi)$ by the functional form given on the right hand side of Eq. 4. The resulting fits and extracted distribution $P_t(\phi)$ are given by the solid and dot-dashed curves in left hand side of Fig. 3, respectively.

The above arguments can be generalized to assess the relative accuracy of reaction plane determinations by the fission and transverse momentum tensor methods for events in which two fission fragments are detected in the exit channel. Figure 4 shows the distributions, $P(\Delta\Phi)$, for the relative orientations of planes determined from two half subsets of detected particles [$P(\Delta\Phi_{12})$, solid points]; from one half-subset and fission fragments, [$P(\Delta\Phi_{F\text{-}1})$, star shaped points]; from fission fragments and the full set of N=4-9 detected particles [$P(\Delta\Phi_{F\text{-}N})$, open squares]. In order to obtain estimates of the primary distributions [$P_{N/2}(\Delta\Phi)$, $P_N(\Delta\Phi)$, $P_F(\Delta\Phi)$] of the experimentally determined planes with respect to the true reaction plane, we assume that the relative orientations between two planes A and B can be described by convolutions of the form

$$P(\Delta\Phi_{A\text{-}B}) = \int P_A(\Phi)P_B(\Phi+\Delta\Phi_{A\text{-}B})d\Phi . \qquad (6)$$

where $P_A(\Phi)$ and $P_B(\Phi)$ denote the probability distributions for the angle Φ between the true reaction plane and the planes A and B, respectively. The dashed curves in Fig. 4 show the convolutions of the individual reaction plane distributions, Eq. (6). From the convolution of the two half-sets, we extracted the shape of the distribution $P_{N/2}(\Delta\Phi_\circ$, shown by the dot-dashed curve. Using this information, we estimated the shape of the distribution, $P_F(\Delta\Phi)$, of fission plane orientations (dotted curve) from the relative distributions of the planes extracted for one half-subset and from fission. Finally, we made an estimate of the shape of the distribution, $P_N(\Delta\Phi)$, of planes extracted from all detected particles. As might have been expected, the estimated distributions $P_N(\Delta\Phi)$ and $P_F(\Delta\Phi)$ have similar azimuthal anisotropies from the present reaction, in qualitative agreement with the

observations of Ref. 2.

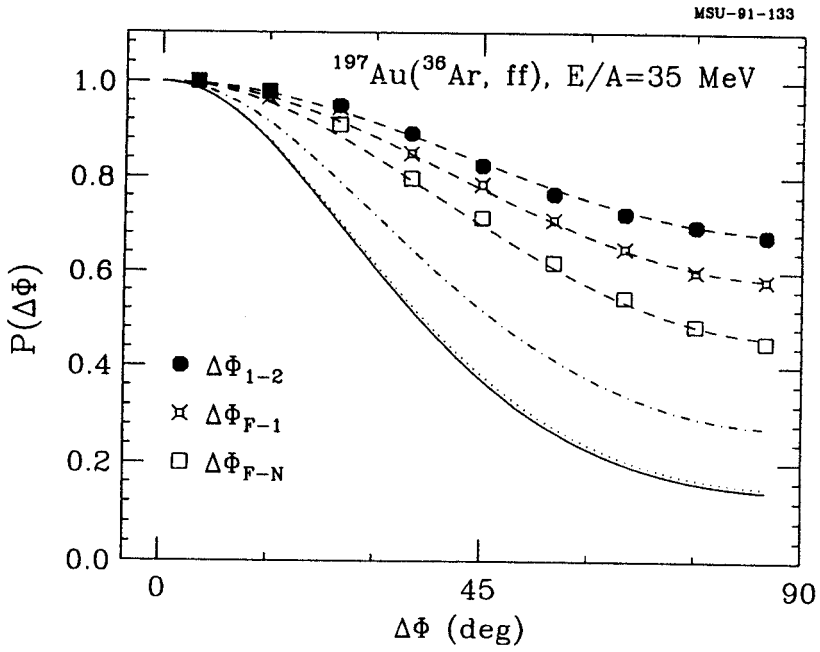

Figure 4: Distributions for the relative orientations of planes determined from two half-subsets for detected particles (solid points), from one such half-subset and from fission (star shaped points), and from the full set of detected particles and from fission (open squares). See text for explanation of the curves.

Summary

Very similar azimuthal correlations were observed with respect to the fission plane and with respect to the plane defined by the orientation of the major axis of the transverse momentum tensor. In situations in which the transverse momentum tensor method is close to optimal, one can obtain reasonably accurate information about the resolution of reaction plane reconstructions by dividing events into two parts, each with half of the original multiplicity, and determining the probability distribution of the angle between the reaction planes determined for each of these subsets. From this experimental probability distribution, one can unfold the resolution of reaction plane reconstructions from each of these parts in a fairly model independent fashion.

a. Instituto de Física, Universidade de São Paulo, C. Postal 20516, CEP 01498, São Paulo, Brazil
b. Indiana University Cyclotron Facility and Department of Chemistry, Indiana University, Bloomington, IN 47405

References

1. C. A. Ogilvie, W. Bauer, D.A. Cebra, J. Clayton, S. Howden, J. Karn, A. Nadasen, A. Vander Molen, G.D. Westfall, W.K. Wilson, and J.S. Winfield, Phys. Rev. C 42, 10 (1990).
2. G.M. Welke, M. Prakash, T>T>S> Kuo, S. Das Gupta, and C. Gale, Phys. Rev. C38, 2101 (1988).
3. M.B. Tsang, C.B. Chitwood, D.J. Fields, C.K. Gelbke, D.R. Klesch, W.G. Lynch, K. Kwiatkowski and

V.E. Viola, Jr., Phys. Rev. Lett. 52, 1967 (1984).
4. M.B. Tsang, Y.D. Kim, Z. Chen, C.K. Gelbke, W.G. Gong, W.G. Lynch, T. Murakami, T. Nayak, R.M. Ronningen, H.M. Xu, F. Zhu, L.G. Sobotka, D.W. Stracener, D.G. Sarantites, Z. Majka, and V. Abenante, Phys. Rev. C42, 15 (1990).
5. W.K. Wilson, W. Benenson, D.A. Cebra, J. Clayton, S. Howden, J. Karn, T. Li, C.A. Ogilvie, A. Vander Molen, G.D. Westfall, J.S. Winfield, and A. Nadasen, Phys. Rev. C41, R1881 (1990).
6. M.B. Tsang, R.T. de Souza, Y.D. Kim, D.R. Bowman, N. Carlin, C.K. Gelbke, W.G. Gong, W.G. Lynch, L. Phair, and F. Zhu, Phys. Rev. C44, 2065 (1991).
7. R.T. de Souza, N. Carlin, Y.D. Kim, J. Ottarson, L. Phair, D.R. Bowman, C.K. Gelbke, W.G. Gong, W.G. Lynch, R.A. Pelak, T. Peterson, G. Poggi, M.B. Tsang, and H.M. Xu, Nucl. Instr. and Meth. A295, 109 (1990).
8. Y.D. Kim, R.T. de Souza, D.R. Bowman, N. Carlin, C.K. Gelbke, W.G. Gong, W.G. Lynch, L. Phair, M.B. Tsang, and F. Zhu, Phys. Rev. C45, 338 (1992).
9. M.B. Tsang, P. Danielewicz, Y.D. Kim, D.R. Bowman, N. Carlin, C.K. Gelbke, W.G. Gong, W.G. Lynch, L. Phair, R.T. de Souza, and F. Zhu, NSCL Annual Report (1991).
10. P. Danielewicz and G. Odyniec, Phys. Lett. B157, 146 (1985).

REACTION DYNAMICS AND DEUTERON PRODUCTION

M.B. Tsang, P. Danielewicz, D.R. Bowman, N. Carlin[a], C.K. Gelbke, Y.D. Kim[b], W.G. Lynch, L. Phair, R.T. de Souza[b], and F. Zhu

Following the tranverse mometum tensor method described in ref [1,2], one can extract the resolution of the experimental reaction plane determination from the data and unfold the measured azimuthal distributions to obtain distributions with respect to the "true" reaction plane. By relating the charged particle multiplicity to the impact parameter of the collision, one can study impact parameter (or multiplicity) selected experimental azimuthal distributions for protons *and* deuterons with microscopic calculations based upon the BUU theory [3,4].

The experiment was performed with a 35 MeV/nucleon ^{36}Ar beam from the K1200 cyclotron of Michigan State University bombarding a ^{197}Au target of 1 mg/cm^2 areal density. Charged particles were detected with the MSU Miniball [5], a plastic-CsI(Tl) scintillator phoswich detector array which covered angles of $16^o \le \theta_{lab} \le 160^o$, corresponding to 85% of 4π. Isotopic identification was achieved for p, d, t, ^{3}He, and ^{4}He. Heavier particles were identified by atomic number up to Z≈20. Representative energy thresholds for identified particles are E_{th}/A≈2, 3, and 4 MeV for He, Ne, and Ar, respectively. Further experimental details are given in refs.[5,6].

To allow a compact presentation of the multiplicity dependence of the azimuthal distributions, we have determined the root mean square of the variances of the true distributions $P_t(d)$:

$$\langle\phi^2\rangle^{1/2} = [\int_0^{\pi/2}\phi^2 P_t(\phi)d\phi / \int_0^{\pi/2} P(\phi)d\phi]^{1/2} \qquad (1)$$

where the integration is over the interval $0 \le \phi \le \pi/2$. For narrow distributions of the form given in Eq. 1, $\langle\phi^2\rangle^{1/2} << \pi/2$, the root mean square of the variance and the width at half maximum, $\phi_{1/2}$, are trivially related: $\phi_{1/2} \sim 1.18\langle\phi^2\rangle^{1/2}$. For simplicity, $\langle\phi^2\rangle^{1/2}$ will be called the azimuthal width in the remaining of this paper.

The azimuthal width of the "true" distributions $P_t(\phi)$ with respect to the true reaction plane for high energy protons (E_p > 32 MeV) and deuterons (E_d > 40 MeV) emitted at $\theta=45^o$ and 72.5^oas a function of charge particle multiplicities are shown as solid points in Fig. 1. Following ref. 6, we have assumed a monotonic relationship between charged particle multiplicity and impact parameter; the corresponding impact parameters are given as the upper scale of Fig. 1. For both protons and deuterons, the extracted azimuthal widths increase with charged particle multiplicity indicating increasingly isotropic distributions for decreasing impact parameters. Qualitatively this trend is

expected. For impact parameter b=0, the emission must be azimuthally isotropic. However, the extracted azimuthal widths of the deuteron distributions at large N are smaller than $<\phi^2>^{1/2} \approx 52^0$, the azimuthal width of an isotropic distribution. This discrepancy may reflect some imprecision in the impact parameter selection.

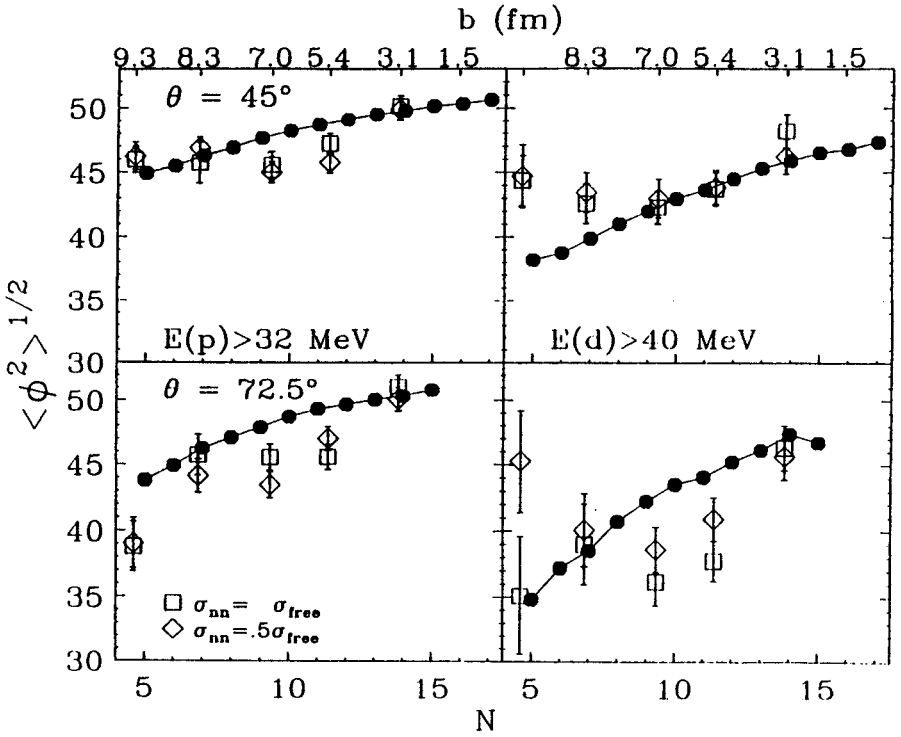

Figure 1: Solid points : Multiplicity dependence of true azimuthal widths of protons (left hand panels) and deuterons (right hand panels) emitted at $\theta=45^0$ (top panels) and $\phi=72.5^0$ (bottom panels). Open points: impact parameter dependence predicted by BUU calculations using a stiff equation of state and $\sigma_{nn} = 0.5\ \sigma_{free}$ (diamonds) and $\sigma_{nn} = \sigma_{free}$ (squares). The multiplicity and impact parameter scales in the figure are related according to the geometrical prescription of ref. [6].

To explore whether the extracted azimuthal width can be reproduced by microscopic transport models, we performed calculations within the framework of a modified BUU model [4] capable of predicting proton *and* deuteron production. This model provides reasonable descriptions of d/p ratios and of spectra at bombarding energies of 100 MeV$\lesssim$E/A$\lesssim$2 GeV [4]. As in other work [3,4,6,7], we adopted a parametrization of the optical potential in terms of a local density, representing a soft equation of state (EOS) with compressibility K=200 MeV. Coulomb interactions were taken into account. The elastic in-medium nucleon-nucleon cross section was taken as the experimental free nucleon-nucleon scattering cross section. The calculations were terminated at the collision time of 220 fm/c. The emitted protons and deuterons were subsequently Coulomb accelerated according to the local Coulomb field which was assumed to be time independent in the center-of-momentum system. For particles with

energies near the semi-classical Coulomb barrier, this approximation provides Coulomb trajectories which differ slightly from the exact trajectories. The approximation is however reasonably accurate for protons and deuterons with energies above the energy cuts used in the angular correlations shown in Fig. 1.

The predicted azimuthal widths of protons and deuterons are shown as open squares and open diamonds using $\sigma_{nn}=\sigma_{free}$ and $\sigma_{nn}=.5*\sigma_{free}$, respectively. The calculations were performed for the impact parameters given by the top scale. The predicted azimuthal widths which are free from normalization uncertainties, are comparable in magnitude to those experimentally observed. Like the experimental data, the calculations predict smaller $<\phi^2>^{1/2}$ for deuterons than for protons, and smaller $<\phi^2>^{1/2}$ at backward angles than for forward angles. Nevertheless, the calculations quantitatively disagree with the data and, in particular, predict a more gradual dependence of $<\phi^2>^{1/2}$ upon b for b > 4 fm than is observed. While some uncertainty exixts with regards to the relation between the multiplicity and the impact parameter, impact parameter averaging the calculations will not change the trends at b>4 fm where the calculations depend less strongly upon the impact parameter than do the data. Since the differences between the two sets of calculations are comparable to the differeences between experiment and theory,different choices of the transport model parameters or a different treatment of the mean field in the nuclear surface may help to reconcile these descrepances. Due to large amounts of computer time required, however, further investigations of model sensitivities lie beyond the scope of the present paper.

In summary, proton and deuteron azimuthal distributions for ^{36}Ar induced reactions on ^{197}Au have been measured relative to the entrance channel reaction plane. These distributions are strongly enhanced in the reaction plane for peripheral collisions, but become more isotropic for central collisions. BUU calculations indicate that Coulomb interactions cannot be neglected in quantitative comparisons with experimental data. While the present calculations reproduce the overall magnitude of the observed azimuthal anisotropies, some quantitative discrepancies remain.

a. Present address: Instituto de Física, Universidade de São Paulo, C. Postal 20516, CEP 01498, São Paulo, Brazil
b. Present address: Indiana University Cyclotron Facility and Department of Chemistry, Indiana University, Bloomington, IN 47405

References

1. M.B. Tsang, R.T. de Souza, Y.D. Kim, D.R. Bowman, N. Carlin, C.K. Gelbke, W.G. Gong, W.G. Lynch, L. Phair, and F. Zhu, NSCL annual report, Pg. xxx (1991).
2. M.B. Tsang, R.T. de Souza, Y.D. Kim, D.R. Bowman, N. Carlin, C.K. Gelbke, W.G. Gong, W.G. Lynch, L. Phair, and F. Zhu, Phys. Rev. C44, 2065 (1991).

3. G.F. Bertsch and S. Das Gupta, Phys. Rep. 160, 189 (1988), and refs. given there.
4. P. Danielewicz and G.F. Bertsch, Nucl. Phys. A533, 712 (1991).
5. R.T. de Souza, N. Carlin, Y.D. Kim, J. Ottarson, L. Phair, D.R. Bowman, C.K. Gelbke, W.G. Gong, W.G. Lynch, R.A. Pelak, T. Peterson, G. Poggi, M.B. Tsang, and H.M. Xu, Nucl. Instr. and Meth. A295, 109 (1990).
6. Y.D. Kim, R.T. de Souza, D.R. Bowman, N. Carlin, C.K. Gelbke, W.G. Gong, W.G. Lynch, L. Phair, M.B. Tsang, and F. Zhu, Phys. Rev. C45, 338 (1992).
7. M.B. Tsang, G.F. Bertsch, W.G. Lynch, and M. Tohyama, Phys. Rev. C40, 1685 (1989).

THERMALIZATION IN NUCLEUS-NUCLEUS COLLISIONS

F. Zhu, W.G. Lynch, D.R. Bowman, R.T. de Souza,C.K. Gelbke, Y.D. Kim, L. Phair, M.B. Tsang, C. Williams, H.M. Xu, and J. Dinius

In energetic nucleus-nucleus collisions, very hot and dilute nuclear systems can be created which decay on time scales commensurate with nuclear relaxation times.[1-5] These transient excitations offer singular opportunities for determining the statistical properties of hot nuclei[2,3] and hot nuclear matter.[4-8] Comparisons of such reactions to statistical theories are often based upon the assumption that the hot nuclear system attains local thermal equilibrium.[4,5] A recent test of this assumption, however, revealed non-thermal populations of the excited states of emitted intermediate mass fragments (Z=3-8), an effect most clearly manifested by inversions in the excited state populations of emitted ^{10}B fragments.[9,10] To investigate whether this observation may be related to the dominance of large impact parameter collisions by non-equilibrium transport phenomena,[11-14] we measured ^{10}B excited state populations in conjunction with a charged particle multiplicity filter.

The experiment was done by bombarding a 1.0 mg/cm^2 ^{197}Au target with a 1260 MeV ^{36}Ar beam produced by the K500 cyclotron of the National Superconducting Cyclotron Laboratory of Michigan State University. The decays of particle unstable intermediate mass fragments (IMF's : Z=3-20) were detected by a tetragonal hodoscope of 13 telescopes,[15] centered at Θ_{lab}= 39°. Nine telescopes, each having a solid angle of 3.6 msr, and consisting of an x-y position sensitive proportional counter, a planar 150 μm silicon surface barrier detector, a 5 mm lithium drift silicon detector, and a 400 μm silicon surface barrier veto counter, were used for the detection of light particles. The four remaining telescopes, each having a solid angle of 5.6 msr and consisting of an x-y position sensitive proportional counter, planar 75 and 100 μm thick surface barrier detectors, and a 5 mm lithium drift silicon detector, were used for the detection of intermediate mass fragments. Energy calibrations, accurate to 1%, were obtained from an ^{241}Am source and a calibrated pulser.

The multiplicity of associated charged particles was measured with rings 2-11 of the MSU Miniball phoswich detector array,[16] which spanned polar angles of 16°≤θ≤160°. To accommodate the hodoscope, 27 of the original 176 phoswich detectors of rings 2-11 were removed; the remaining array covered approximately 77% of 4π. Charged particles were identified by element for Z≈1-20 in the Miniball, with thresholds of 2, 3, and 4 MeV/nucleon for Z=3, 10, and 18 fragments, respectively. Further details of the Miniball detection array are provided in refs. [16,17].

Measured charged particle multiplicity distributions are shown in the upper right corner of Figure 1.[18] The solid points indicate the probability of observing the charged particle

multiplicity, N_A, in the Miniball associated with the detection of a ^{10}B nucleus in the hodoscope. The dashed line indicates the corresponding inclusive multiplicity distribution.[18] The impact parameter scale in the figure was estimated by assuming a monotonic relation between the impact parameter and the associated multiplicity.[17] Consistent with previous observations,[17,19] the detection of one ^{10}B fragment in the hodoscope suppresses peripheral collisions significantly. Gates, indicated by the dashed-dotted lines, were used to distinguish "peripheral" ($N_A \leq 5$) and "central" collisions ($N_A \geq 10$) collisions. Energy spectra for particle stable ^{10}B fragments for these two multiplicity bins are shown in the remainder of Figure 1. The spectra for central collisions have steeper slopes than those obtained for peripheral collisions, reflecting a more complete dissipation of the incident energy into other degrees of freedom.

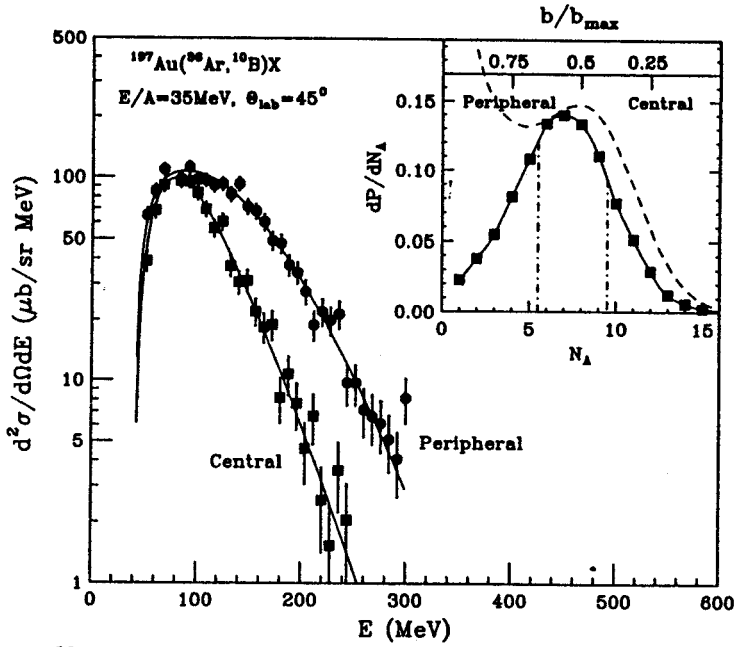

Figure 1: Energy spectra for ^{10}B nuclei detected at 45° in the high resolution hodoscope, for low multiplicity (solid points) and high multiplicity (solid squares) gates on the Miniball. The solid lines denote moving source fits, used in the efficiency calculations. The solid points (connected by a solid curve) in the insert are the measured probability distribution for the associate multiplicity of charged particles in coincidence with ^{10}B nuclei detected in the high resolution hodoscope. The dashed line depicts the inclusive multiplicity distribution, normalized arbitrarily. The dashed-dotted lines depict the boundaries of the multiplicity gates described in the text.

The relative populations of particle unstable states in ^{10}B nuclei were measured by detecting the coincident decay products. These yields are shown as a function of excitation energy for the $^{10}B^* \rightarrow {}^6Li+\alpha$ and $^{10}B^* \rightarrow {}^9Be+p$ decay channels in the upper and lower halves of Figure 2, respectively. Spectra obtained for peripheral and central collisions are shown in the left and right sides of the figure, respectively. The separation energy E_b for each decay channel and the locations and spins of

the relevant particle unstable excited states of ^{10}B nuclei are indicated in the left hand panels of the figure.[20] In comparison to lower lying particle unbound states, the group of states at about 6 MeV excitation energy is more strongly populated in less violent "peripheral" collisions than in more violent "central" collisions.

The $^{6}Li+\alpha$ and $^{9}Be+p$ coincidence yields consist of a contribution, Y_c, from the decay of particle unstable ^{10}B nuclei into channel c and a background, Y_b. This background has been parameterized by [15]

$$Y_b = C_{12} Y_1 Y_2 \{1 - \exp[-(E^* - E_b)/\Delta_b]\}, \quad (1)$$

where Δ_b governs the width of the minimum caused by the Coulomb repulsion between the two fragments; C_{12} is a fit parameter; and Y_1 and Y_2 are the measured inclusive yields for particles 1 and 2, gated by the appropriate charged particle multiplicity.

The measured yield $Y_c(E^*)$ from the decay of particle unstable ^{10}B nuclei is a function of the population probabilities n_i and the detection efficiency of the hodoscope. Details of the calculation of the efficiency function are provided in ref. [15].

The population probabilities, n_i, were extracted by fitting the coincidence yield with a superposition of Breit-Wigner lines corresponding to the states indicated in the left panels of Figure 2 for different assumptions of the background parameter Δ_b. Reasonable fits were obtained for backgrounds lying within the values bounded by the dashed lines in Figure 2. The population probabilities, n_i, were assumed to be the same within those groups of states in Figure 2 which were not resolved. The best fits to the coincidence yields are shown by the solid curves in Figure 2.

Figure 3 shows the measured population probabilities as a function of excitation energy for peripheral (left side) and central (right side) collisions. The error bars include the uncertainties in the background subtraction bounded by the two assumed background coincidence yields displayed in Figure 2. In thermal as well as many statistical models, the initial excited state population probabilities of intermediate mass fragments should be proportional to a Boltzmann factor, $\exp(-E^*/T_{eff})$ where T_{eff} is the effective temperature of the system at breakup. The dashed lines in Fig. 3 show the exponential dependence dictated by the Boltzmann factor for T_{eff} = 4 MeV. For peripheral collisions, the measured relative populations deviate significantly from the expected monotonic behavior and a population inversion is observed; the group of states at E^*=6.0 MeV is populated much more strongly than the lower lying states at 5.2 and 4.8 MeV. Such effects were already observed in the inclusive measurements of ref. [9]. The inversions disappear for central collisions. The

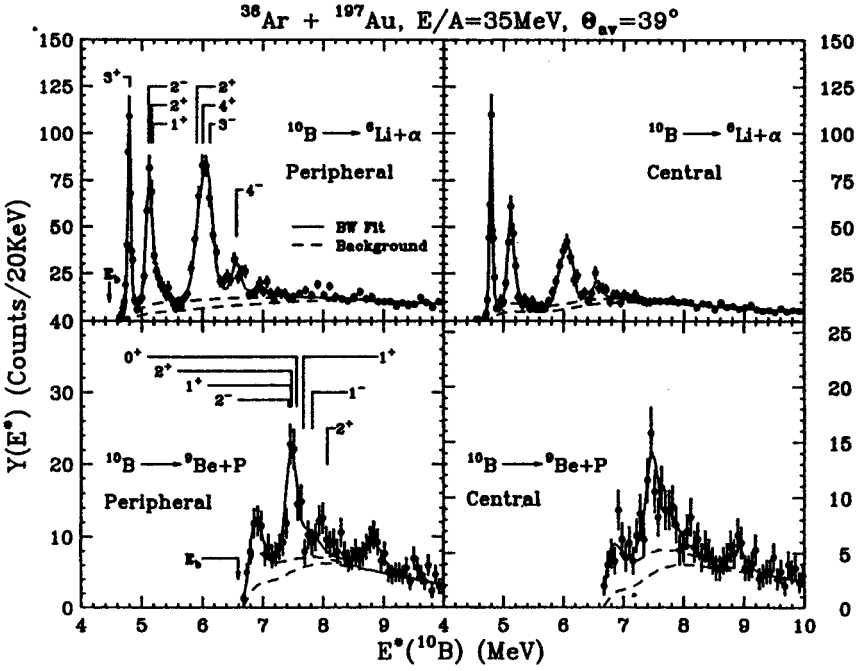

Figure 2: Yields for the decays: $^{10}B \rightarrow {}^{6}Li + \alpha$ (upper half) and $^{10}B \rightarrow {}^{9}Be + p$ (lower half). Spectra obtained for peripheral and central collisions are shown on the left and right hand sides, respectively. The curves are described in the text.

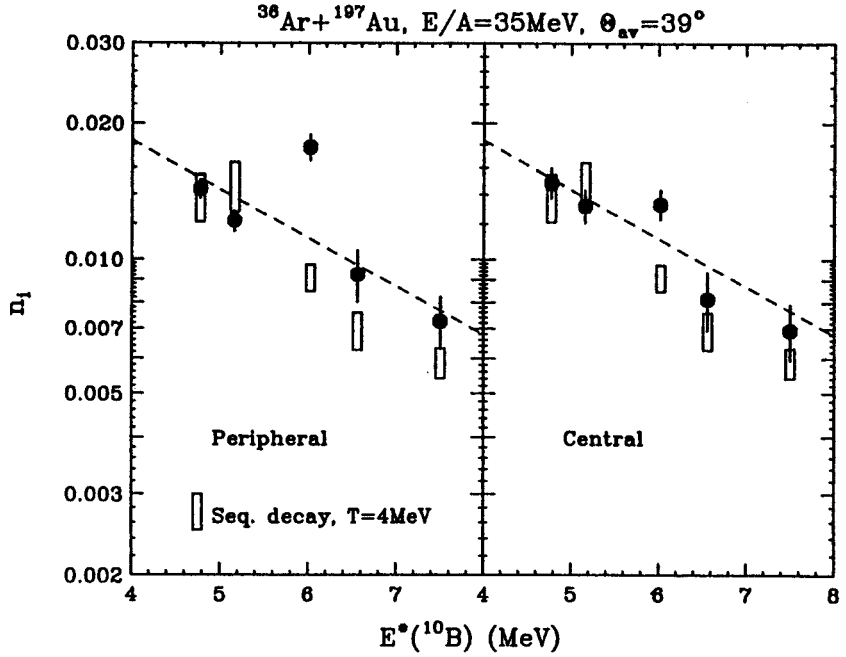

Figure 3: The solid points designate population probabilities for the excited states of ^{10}B nuclei measured for peripheral (left side) and central (right side) collisions. The open bars indicate the results of the sequential decay calculations. The solid lines denote exponentials $\exp(E^*/T_{eff})$ with T_{eff}= 4 MeV.

population probabilities, however, do not fall off exponentially as expected from the Boltzmann factor; instead, one observes an approximately constant population probability for the 5.2 and 6.0 MeV levels.

The initial populations of excited states will be modified by the sequential feeding from heavier particle unstable nuclei. These feeding corrections have been estimated via calculations in which it is assumed that the excited states of primary emitted fragments are populated thermally; the initial elemental yields are subject to a constraint that the final elemental distributions are consistent with the measured elemental distributions.[9,10] In these calculations, decays were calculated from the Hauser-Feshbach theory[21] with parity and isospin conservation taken into account; known branching ratios[22] were used when available. Unknown spins or parities of low lying discrete states were assigned randomly and calculations repeated with different spin assignments until sensitivities of the population probabilities to these uncertainties could be assessed.

In order to provide an overall comparison between the calculated and measured population probabilities, a least squares analysis was performed by computing

$$X^2_\nu(T) = \frac{1}{\nu}\sum_{i=1}^{\nu} \frac{(n_{exp,i} - n(T)_{cal,i})^2}{\sigma^2_{exp,i} + \sigma^2_{cal,i}}, \quad (4)$$

for a range of initial emission temperatures. Here, $n_{exp,i}$ and $n(T)_{cal,i}$ are the measured and calculated population probabilities and $\sigma_{exp,i}$ and $\sigma_{cal,i}$ are the corresponding uncertainties. The resulting values of $X^2_\nu(T)$ are shown in Table 1. Optimal agreement between calculated and measured population probabilities is obtained for both central and peripheral collisions at temperatures of about T ≈ 3-5 MeV. Similar residue temperatures have been obtained in dynamical[23,24] and in statistical[25-28] calculations. For T = 4 MeV, the population probabilities obtained by the sequential decay calculations are indicated by the open bars in the Figure 3; the vertical extent of the bars graphically demonstrates the range of theoretical values obtained for ten randomly chosen assumptions about the unknown spins of low lying discete states. (Rotational effects may add comparable contributions to the uncertainties in the calculated population probabilities.[10]) The population probabilities obtained from the sequential decay calculations cannot be reconciled with the population inversions observed for peripheral collisions. For central collisions, on the other hand, the discrepancies between calculated and measured population probabilities are much smaller, but still too large for a purely thermal interpretation.

At present, there is no definitive explanation for enhanced populations of specific states like those contained in the group at E^* = 6 MeV. Such effects can arise from non-statistical population

mechanisms or from statistical feeding which is governed by branching ratios that differ significantly from those assumed in the Hauser-Feshbach model.[10] The experimental trends in Figure 3 suggest that such effects diminish as the number of alternative decay paths increase.

T (MeV)	χ^2_ν(Peripheral)	χ^2_ν(Central)
2	55.5	30.3
3	14.2	3.14
4	10.3	2.41
5	9.35	2.77
6	17.5	7.12

Table 1: Values for X^2_ν(T) are calculated, according to Eq. 4, for temperatures ranging from 2 to 6 MeV.

References

1. C.K. Gelbke, and D.H. Boal, Prog. Part. Nucl. Phys. 19 (1987) 33, and references contained therein.
2. E. Suraud, C. Grégoire, and B. Tamain, Prog. Part. Nucl. Phys. 23 (1989) 357, and references contained therein.
3. D. Guerreau, "Nuclear Matter and Heavy Ion Collisions", Plenum Press, Nato ASI Series B 205 (1989) 187, and references contained therein.
4. L.P. Csernai, and J.I. Kapusta, Phys. Rep. 131 (1986) 223, and references contained therein.
5. W.G. Lynch, Ann. Rev. Nucl. Part. Sci. 37 (1987) 493, and references contained therein.
6. R.T. de Souza, L. Phair, D.R. Bowman, N. Carlin, C.K. Gelbke, W.G. Gong, Y.D. Kim, M.A. Lisa, W.G. Lynch, G.F. Peaslee, M.B. Tsang, H.M. Xu, and F. Zhu, Phys. Lett. B 268 (1991) 6.
7. D.R. Bowman, G.F. Peaslee, R.T. de Souza, N. Carlin, C.K. Gelbke, W.G. Gong, Y.D. Kim, M.A. Lisa, W.G. Lynch, L. Phair, M.B. Tsang, C. Williams, Phys. Rev. Lett. 67 (1991) 1527.
8. C.A. Ogilvie, J.C. Adloff, M. Begemann-Blaich, P. Bouissou, J. Hubele, G. Imme, I. Iori, P. Kreutz, G.J. Kunde, S. Leray, V. Lindenstruth, Z. Liu, U. Lynen, R.J. Meijer, U. Milkau, W.F.J. Müller, C. Ngô, J. Pochodzalla, G. Raciti, G. Rudolf, H. Sann, A. Schüttauf, W. Seidel, L. Stuttge, W. Trautmann, and A. Tucholski, Phys. Rev. Lett. 67 (1991) 1214.
9. T.K. Nayak, T. Murakami, W.G. Lynch, K. Swartz, D.J. Fields, C.K. Gelbke, Y.D. Kim, J. Pochodzalla, M.B. Tsang, H.M. Xu, F. Zhu, and K. Kwiatkowski, Phys. Rev. Lett. 62 (1989) 1021.
10. T.K. Nayak, T. Murakami, W.G. Lynch, K. Swartz, D.J. Fields, C.K. Gelbke, Y.D. Kim, J. Pochodzalla, M.B. Tsang, H.M. Xu, F. Zhu, and K. Kwiatkowski, Phys. Rev. C45, 132.
11. T.C. Awes, R.L. Ferguson, R. Novotny, F.E. Obenshain, F. Plasil, S. Pontoppidan, V. Rauch, G.R. Young, and H. Sann, Phys. Rev. Lett. 52 (1984) 251.
12. R. Vandenbosch, A. Lazzarini, D. Leach, D.K. lock, A. Ray, and A. Seamster, Phys. Rev. Lett. 52 (1984) 1964.
13. J. Randrup, Nucl. Phys. A307 (1978) 319; A327 (1979) 490.
14. T. Døssing and J. Randrup, Nucl. Phys. A433 (1985) 215; A433 (1985) 280.

15. T. Murakami, T.K. Nayak, W.G. Lynch, K. Swartz, Z. Chen, D.J. Fields, C.K. Gelbke, Y.D. Kim, M.R. Maier, J. Pochodzalla, M.B. Tsang, H.M. Xu, and F. Zhu, Nucl. Instr. and Meth. A275 (1989) 112.
16. R.T. DeSouza, N. Carlin, Y.D. Kim, J. Ottarson, L. Phair, D.R. Bowman, C.K. Gelbke, W.G. Gong, W.G. Lynch, R.A. Pelak, T. Peterson, G. Poggi, M.B. Tsang, and H.M. Xu, Nucl. Instr. and Meth. A295 (1990) 109.
17. Y.D. Kim, R.T. de Souza, D.R. Bowman, N. Carlin, C.K. Gelbke, W.G. Gong, W.G. Lynch, L. Phair, M.B. Tsang, and F. Zhu, Phys. Rev. C. in press.
18. This is the multiplicity detected in the 149 active Miniball elements, not the multiplicity [17] which would be detected in the complete array.
19. Y.D. Kim, M.B. Tsang, C.K. Gelbke, W.G. Lynch, N. Carlin, Z. Chen, R. Fox, W.G. Gong, T. Murakami, T.K. Nayak, R.M. Ronningen, H.M. Xu, F. Zhu, W. Bauer, L.G. Sobotka, D. Stracener, D.G. Sarantites, Z. Majka, V. Abenante, and H. Griffin, Phys. Rev. Lett. 63 (1989) 494.
20. Additional states at E = 7.67, 7.819, 8.07, 8.7, 8.889 and 8.895 MeV were included in the fit, but were characterized by populations which were statistically insignificant, though consistent with an emission temperature of about 4 MeV. The structure at 7 MeV in the ^{8}Be+p spectrum reflects contributions from excited states at 6.873 and 7.002 MeV which have poorly known proton branching ratios, superimposed upon a prominent peak in the detection efficiency of the hodoscope.
21. W. Hauser and H. Feshbach, Phys. Rev. 87 (1952) 366.
22. F. Ajzenberg-Selove, Nucl. Phys. A475 (1987) 1; A413 (1984) 1; A433 (1985) 1; A449 (1986) 1; A460 (1986) 1.
23. H.M. Xu, P. Danielewicz, and W.G. Lynch, to be published.
24. D. Boal, J. Glosli, and C. Wicentowich, Phys. Rev. C40 (1989) 601.
25. S. Levit and P. Bonche, Nucl. Phys. A437 (1984) 426.
26. D.H.E. Gross, Phys. Lett. B203 (1988) 26.
27. J.P. Bondorf, R. Donangelo, L.N. Mishustin, C.J. Pethick, H.Schulz and K. Sneppen, Nucl. Phys. A443 (1985) 321.
28. W.A. Friedman, Phys. Rev. Lett. 60 (1988) 2125.

CLASSICAL APPROXIMATION FOR THE CALCULATION OF TWO-PROTON CORRELATION FUNCTIONS FOR EMISSIONS WITH LONG LIFETIMES

W.G. Gong, Y.D. Kim, and C.K. Gelbke

Two-proton correlation functions are sensitive to time scales of evaporative emission processes[1-6]. Two different techniques have been used for numerical calculations. One technique is based upon the Koonin-Pratt formula[7-9], and the other employs classical trajectory calculations[1,2,5]. As it is not clear whether and under which conditions the two approaches yield similar (or identical) results, we have performed numerical calculations for a simplified source function and test the approximations underlying these theoretical treatments.

For simplicity, we used a schematic source function corresponding to thermal emission from the surface of a sharp sphere of radius R:

$$g(\vec{p},\vec{r},t) \propto (\hat{r}\cdot\hat{p})\Theta(\hat{r}\cdot\hat{p})\delta(r-R_S)\Theta(E-V_S)(E-V_S)e^{-(E-V_S)/T}e^{-t/\tau}. \qquad (1)$$

Here, $g(\vec{p},\vec{r},t)$ denotes the probability density of emitting a particle of momentum $\vec{p}$ at location $\vec{r}$ and time t; $\Theta(x)$ is the unit step function which vanishes for $x<0$; $\delta(x)$ is the delta function; $\hat{r}$ and $\hat{p}$ are unit vectors parallel to $\vec{r}$ and $\vec{p}$; $E=p^2/2m$; T is the temperature parameter; and $V_S=Z_Se^2/R_S$ is the Coulomb barrier. An exponential time dependence is assumed, with energy independent mean emission time τ. We performed calculations for the parameters Z_S=78, R_S=8 fm, T=4 MeV, and τ=200, 500, 1000 fm/c.

The Koonin-Pratt formula[7-9] allows the calculation of the two-particle correlation function in terms of the single-particle phase-space distribution and the relative wave function of the emitted particle pair[8,9]:

$$1+R(\vec{P},\vec{q}) = \int d^3r F_{\vec{P}}(\vec{r})\,|\phi(\vec{q},\vec{r})|^2. \qquad (2)$$

where $\vec{r} = \vec{r}_1-\vec{r}_2$ is the relative coordinate of the emitted particles, and $\vec{P}$ and $\vec{q}$ are the total and relative momenta of the proton pair. The function $F_{\vec{P}}(\vec{r})$ is defined by:

$$F_{\vec{P}}(\vec{r}) = \frac{\int d^3R\, f(\vec{P}/2, \vec{R}+\vec{r}/2, t_>)\, f(\vec{P}/2, \vec{R}-\vec{r}/2, t_>)}{|\int d^3r'\, f(\vec{P}/2, \vec{r}', t_>)|^2}. \qquad (3)$$

where $\vec{R} = \frac{1}{2}(\vec{r}_1+\vec{r}_2)$ is the center-of-mass coordinate of the two particles. The Wigner function $f(\vec{p},\vec{r},t_>)$ is the phase-space distribution of particles of momentum $\vec{p}$ at position $\vec{r}$ at some time, $t_>$, after both particles have been emitted:

$$f(\vec{p},\vec{r},t_>) = \int_{-\infty}^{t_>} dt\, g(\vec{p},\vec{r}-\vec{p}(t_>-t)/m,t) . \qquad (4)$$

If all relative orientations between $\vec{P}$ and $\vec{q}$ are integrated over, the classical approximation to the Eq. 2 can be written as [10]:

$$1+R(\vec{P},\vec{q}) = \int d^3r F_{\vec{P}}(\vec{r})[\,1-me^2/q^2r\,]^{1/2} . \qquad (5)$$

In the Koonin-Pratt formula, the correlation function depends only on the final relative positions of all the particles with momentum $\vec{P}/2$. It is derived [9] under the assumptions that the final-state interaction between the two protons dominates and that final-state interactions with the remaining system are negligible, that the single particle phase space distribution varies only slowly over particle momenta ½P±q, and that the correlation functions are determined by the two-body density of states as corrected by the interactions between the two particles.

We performed trajectory calculations in which the final-state Coulomb interaction with the emitting system was incorporated (Z_S=78), or neglected (Z_S=0). In these calculations, recoil effects were taken into account (the mass of the emitting system was taken as M_S=197 u). The emission function in the rest frame of the emitting system (Eq. 1) was sampled by Monte-Carlo techniques. For trajectory calculations in which the Coulomb interaction with the emitting system was taken into account (Z_S=78), the Coulomb parameter in Eq. 1 was set to V_S=0. For calculations in which the Coulomb interaction with the emitting nucleus was turned off, the Coulomb parameter $V_S=78e^2/R_S$ was used in Eq. 1 to ensure close similarity of the asymptotic kinetic energy spectra for all calculations. Upon emission, the particle trajectories were calculated by integrating Newton's equations, and the asymptotic particle momenta were stored as coincidence events and as single-particle spectra. Correlation functions, 1+R(q), were constructed from the calculated coincidence and single-particle yields, $Y_{12}(\vec{p}_1,\vec{p}_2)$ and $Y_i(\vec{p}_i)$, respectively:

$$\Sigma Y_{12}(\vec{p}_1,\vec{p}_2) = C(1+R(q))\,\Sigma Y_1(\vec{p}_1)Y_2(\vec{p}_2) . \qquad (6)$$

The normalization constant C was determined by the requirement that <R(q)>=0 at large relative momenta.

Correlation functions calculated with various approximations are compared in Fig. 1 for a relatively short emission time (τ=200 fm/c). The solid curves represent the correlation functions calculated from the Koonin-Pratt formula, Eqs. 2-4. The dotted curves represent calculations with the Koonin-Pratt formula in which the nuclear p-p interaction was turned off; the relative wave function is then given by the (properly antisymmetrized) Coulomb scattering wave-function for spin-½ particles. Comparison between these two calculations indicates that the nuclear interaction is important.

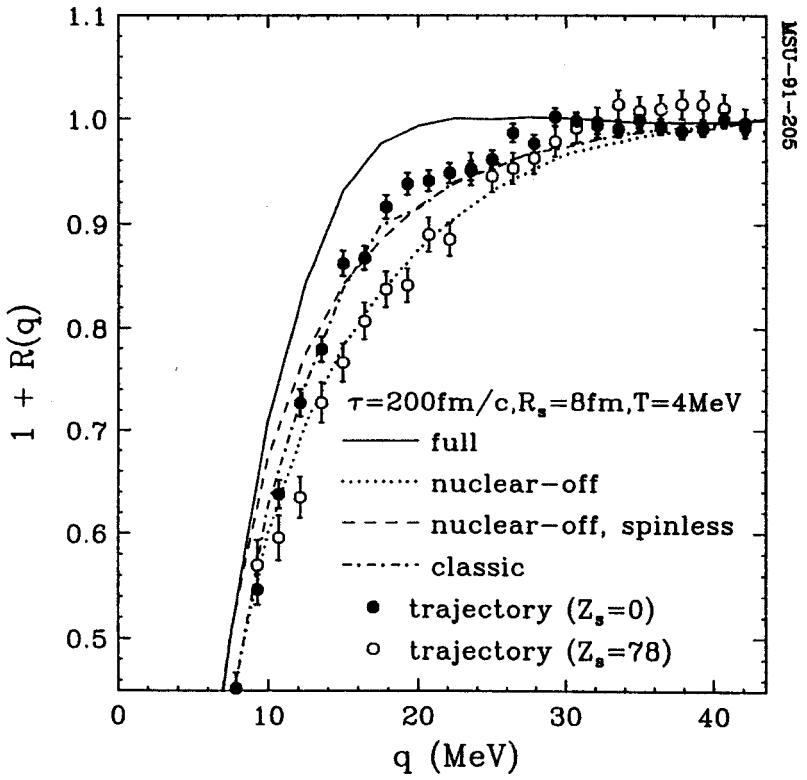

Figure 1. Two proton correlation functions for a schematic source (Eq. 1) representing thermal surface emission with fixed life-time, τ=200 fm/c. The parameters are indicated in the figure. Solid, dotted, and dashed curves were calculated with the Koonin-Pratt formula using the full p-p wavefunction, neglecting the nuclear interaction, and neglecting both nuclear interaction and antisymmetrization. The dot-dashed curve was calculated with Eq. 4. Open and solid points are the results of trajectory calculations with and without treatment of the Coulomb interaction with the emitting source.

The dashed curve in Fig. 1 represents a calculation with the Koonin-Pratt formula in which the two protons are assumed to be spinless and distinguishable particles, i.e. the relative wave function is given by the (non-antisymmetrized) Coulomb scattering wave-function. The dot-dashed curves show the results obtained with the classical approximation [10] to the Koonin-Pratt formula, Eq. 4. The classical approximation provides an excellent approximation for the calculations of angle integrated

correlation functions arising from Coulomb final-state interactions between distinguishable particles, even if they are as light as protons. (Note, however, that antisymmetrization effects cannot be safely neglected.)

The open points in Fig. 1 show the results of classical trajectory calculations incorporating the Coulomb interaction with the emitting system (Z_S=78). For comparison, the solid points show results obtained by turning off the Coulomb interaction with the emitting source (Z_S=0). (These latter calculations are not necessarily identical with results obtained from Eq. 4, as they do not rely on the approximation, implicit in the Koonin-Pratt formula, of using only the one-body phase space density at the center-of-mass velocity of the two-proton pair [10].) For τ=200 fm/c, the differences between the two trajectory calculations are not negligible. (This conclusion depends on the shape of the energy spectrum: Coulomb distortions in the field of the heavy reaction residue decrease for the emission of more energetic protons.)

The results of these and similar calculations for τ=500 and 1000 fm/c lead to the following conclusions: The neglect of the two-proton nuclear interaction and the antisymmetrization of the two-proton wave-function leads to comparable or larger inaccuracies than the neglect of the Coulomb interaction with the emitting heavy residue. For large emission times $\tau \gtrsim 1000$ fm/c, pertinent for the decay of low-temperature compound nuclei, the classical approximation to the Koonin-Pratt formula provides an excellent approximation for the calculation of angle integrated two-proton correlation functions and gives virtually identical results to trajectory calculations.

References

1. P.A. DeYoung et al., Phys. Rev. C39, 128 (1989).
2. P.A. DeYoung et al., Phys. Rev. C41, R1885 (1990).
3. W.G. Gong et al., Phys. Lett. B246, 21 (1990).
4. D. Goujdami et al., Z. Phys. A339, 293 (1991).
5. A. Elmaani et al., Phys. Rev. C43, R2474 (1991).
6. W.G. Gong et al., Phys. Rev. C43, 1804 (1991).
7. For a recent review, see e.g. D.H. Boal, C.K. Gelbke, and B.K. Jennings, Rev. Mod. Phys. 62, 553 (1990).
8. S.E. Koonin, Phys. Lett. 70B, 43 (1977).
9. W.G. Gong et al., Phys. Rev. C43 (1991) 781.
10. Y.D. Kim et al., Phys. Rev. C45 (1992) 387.

MULTIFRAGMENT DISINTEGRATION OF THE $^{129}Xe+^{197}Au$ SYSTEM AT E/A = 50 MeV

D.R. Bowman, G.F. Peaslee, R.T. de Souza, N. Carlin[a], C.K. Gelbke, W.G. Gong, Y.D. Kim, M.A. Lisa, W.G. Lynch, L. Phair, M.B. Tsang, C. Williams, N. Colonna[b], K. Hanold[b], M.A. McMahan[c], G.J. Wozniak[b], L.G. Moretto[b], and W.A. Friedman[d]

Multifragment emission following heavy-ion collisions represents a novel mode of nuclear disassembly[1,2]. While several different theories predict the occurrence of multifragment decay, the underlying physics is not yet clear since experimental information which discriminates between these models is virtually nonexistent. It is still uncertain under what experimental conditions multifragment emission becomes a dominant decay channel. In order to characterize multifragment final states and to test predictions of different fragment production models, we have measured charged particle and intermediate mass fragment (IMF, Z = 3-20) multiplicities for the $^{129}Xe+^{197}Au$ reaction at E_{cm} = 3.9 GeV using a low-threshold 4π charged particle detector[3].

An E/A = 49.8 MeV ^{129}Xe beam with an intensity of 10^7 particles/s impinged upon a 1.05 mg/cm^2 gold target. Reaction products were detected with 171 elements of the MSU Miniball phoswich detector array[3] which subtended polar angles of $16° \le \theta \le 160°$, corresponding to approximately 87% of 4π. The most forward angles were covered by a 16-element hodoscope, each element of which consisted of two position-sensitive solid-state detectors (300 μm and 5 mm thick), and a 7.6 cm thick plastic scintillator[4]. This forward hodoscope covered approximately 64% of the solid angle at $2° \le \theta \le 16°$, or 1.2% of 4π. Fragments detected in the Miniball were identified by atomic number for Z ≈ 1-20; representative detection thresholds were 2, 3, and 4 MeV/nucleon for Z = 3, 10, and 18 fragments, respectively. Fragments detected in the forward array were identified by element for Z = 1-54; representative detection thresholds were 6, 13, 21, and 27 MeV/nucleon for Z = 2, 8, 20, and 54 fragments, respectively.

Experimental charged particle multiplicity distributions (uncorrected for detector acceptance) are shown in Fig. 1. The upper panel shows the probability distribution of N_C, the detected charged particle multiplicity. The lower panel shows probability distributions of N_{IMF}, the number of detected intermediate mass fragments ($3 \le Z \le 20$) for several gates on N_C. The average number of detected IMFs increases with N_C. For the most central gate, $N_C \ge 33$, it reaches a value of $\langle N_{IMF} \rangle = 6.5$[5], which is the largest value yet observed in any nuclear collision. Events with $N_{IMF} = 14$ are observed.

The solid points in Fig. 2 show the average fragment multiplicity, $\langle N_{IMF} \rangle$, as a function of N_C. The average fragment multiplicity increases monotonically from $\langle N_{IMF} \rangle \approx 1$ for $N_C = 10$ to $\langle N_{IMF} \rangle \approx 6.2$ for $N_C = 35$. This monotonic relationship between $\langle N_{IMF} \rangle$ and N_C indicates that IMF emission

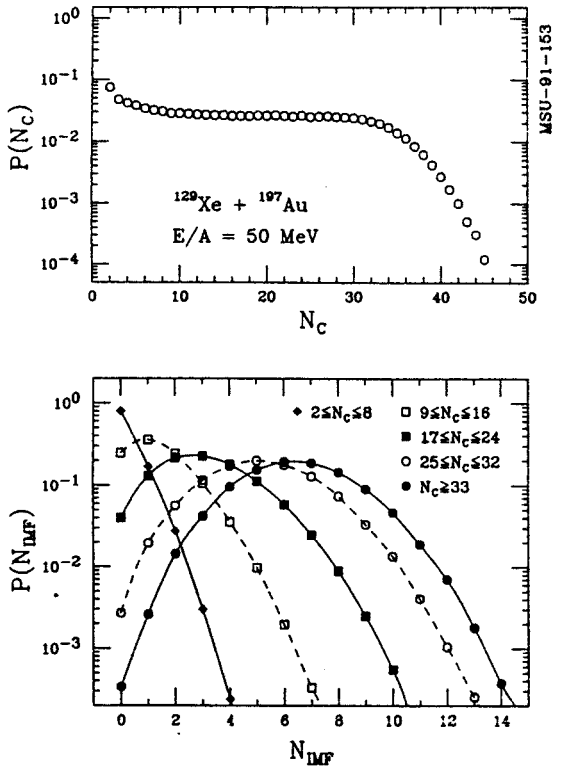

Figure 1: Upper panel: Measured charged particle multiplicity distribution, N_C, for the $^{129}Xe+^{197}Au$ reaction at E/A = 50 MeV. Lower panel: Measured IMF multiplicity distributions for the indicated gates on N_C. All distributions are normalized to unit area.

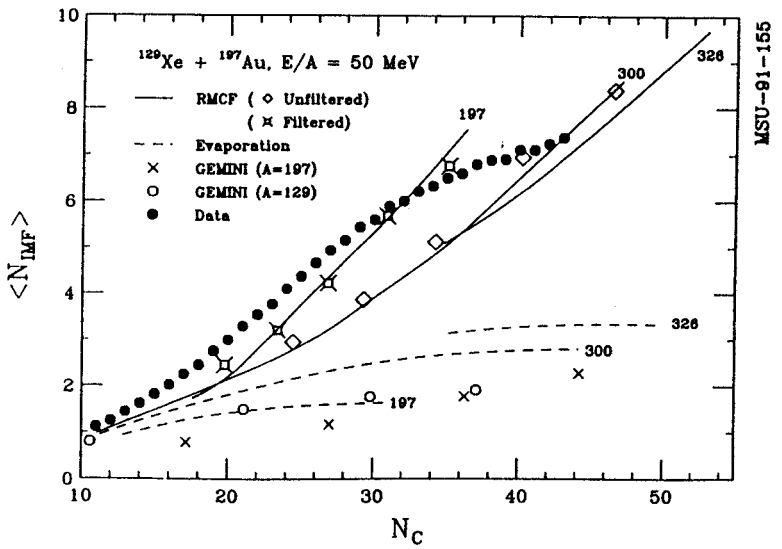

Figure 2: Relation between average IMF and charged particle multiplicities. Solid points represent measured values. Solid and dashed curves are calculated with the models of refs. 11 and 9, respectively, for the indicated initial masses. Crosses and open circular points represent calculations with the model of ref. 8 for the decay of hot ^{129}Xe and ^{197}Au nuclei, respectively. Diamond and star-shaped points illustrate instrumental distortions: diamonds represent assumed primary distributions (from the model of ref. 11), and star shaped points depict corresponding values filtered by the response of the experimental apparatus.

increases with increasing energy deposition, or decreasing impact parameter, or both. We have performed calculations with several types of models to investigate whether they are able to predict the experimental relationship quantitatively.

In view of the possible role of dynamics in this reaction, we have performed calculations with the microscopic quasi-particle dynamics (QPD) model[6], which simulates fragment emission without relying on the assumption of statistical equilibrium. Typical calculations were followed to times of t = 300 fm/c when fast non-equilibrium emission has ceased[7]. In simulations leading to a total charged particle multiplicity of 36-45, the predicted average IMF multiplicities, $\langle N_{IMF} \rangle < 1$, are much smaller than those observed experimentally. At t = 300 fm/c a single, highly excited (E^* =1.5 GeV), heavy residue with Z > 20 is predicted to exist, which then decays on a slower time scale. Calculations followed to times of t = 3000 fm/c, when the heavy residue has cooled, predict slightly fewer fragments due to particle decays of the excited IMFs formed in the earlier stages of the reaction. Thus the large fragment multiplicities observed experimentally are not predicted with this dynamical simulation.

We also investigated an alternative limit of fragment production using models which calculate statistical emission from equilibrated nuclei at normal density[8,9]. Since predictions of statistical models depend on the initial mass, charge, and excitation energy of the excited systems, calculations were performed for a variety of initial conditions. These calculations can give useful information about the influence of phase space on fragment emission, and provide instructive comparisons with dynamical treatment where the phase space limit may not be achieved.

Although limitations in the transition-state formalism do not allow calculations of the decay of fusion products in the $^{129}Xe + ^{197}Au$ reaction, we did investigate a broad range of two-body scenarios in which we consider the statistical decay of highly excited projectile-like and target-like fragments which share the available excitation energy in different proportions. The open circles and crosses in Fig. 2 indicate the multiplicities predicted by the statistical decay code GEMINI[8] for the decay of highly excited ^{129}Xe and ^{197}Au nuclei, respectively, with excitation energies of E*(Xe) = 0.5, 1.0, 1.5, and 2.0 GeV; and E*(Au) = 1.0, 1.5, 2.0, and 2.5 GeV. In the code, all binary mass divisions from light particle evaporation to symmetric fission are considered, and sequential decays of particle unstable primary fragments are incorporated. For each calculation, a level density parameter of a = A/(8.5 MeV) was used, and initial angular momenta of I(Xe) = 87 $\hbar$ and I(Au) = 80 $\hbar$ were assumed (these are the maximum angular momenta for which barriers exist for all decay channels). For large charged particle multiplicity, $N_C \gtrsim 20$, the average IMF multiplicities calculated from the

combined decay of the projectile and target residues is much smaller than observed experimentally, independent of the assumed partition of excitation energy.

We have also investigated a range of incomplete and complete fusion scenarios using a statistical evaporation model[9]. The dashed curves in Fig. 2 depict the predicted multiplicity correlations for initial masses A = 197, 300, and 326. Each curve was constructed by simulating the decay of a particular system at different initial temperatures. None of the calculations can reproduce the large IMF multiplicities measured for $N_C \gtrsim 20$[10].

While these two models are based on different statistical formalisms they make consistent predictions for the relation between $\langle N_{IMF} \rangle$ and N_C, and they both fail to reproduce the large IMF multiplicities measured for $N_C \gtrsim 20$.

The statistical calculations discussed above treat the decay of an excited nucleus at normal nuclear density. Drastically different results are obtained when the hot nucleus is allowed to expand isentropically under the influence of thermal pressure[11]. In this scenario, following an initial stage of energy deposition, the hot residue expands from normal nuclear density. Fragment emission, described by the Weisskopf formalism, increases dramatically if the expansion proceeds to densities $\rho \lesssim 0.4\rho_o$ where Rapid Massive Cluster Formation[11] can occur. This phenomenon is driven by the difference in free energy of the expanded system and the emitted fragments. The solid curves show results of calculations with this model assuming zero initial expansion energy, i.e. no initial compression[12], and a finite-nucleus equation-of-state with compressibility coefficient K = 144 MeV. Evaporation calculations were performed for the same range of masses and temperatures as for the nonexpanding systems[9]. Significantly larger IMF multiplicities are predicted for large values of N_C and the trend with increasing charged particle multiplicity is in reasonable agreement with the data, independent of the assumptions of the mass and charge of the decaying nuclei.

To investigate the influence of detection thresholds and incomplete solid angle coverage on the measured charged particle and IMF multiplicities, we have filtered representative theoretical results with the response of our experimental apparatus. In Fig. 2, the five open diamonds represent raw model predictions[11], and the five star-shaped points show the corresponding values after the response of the experimental apparatus is taken into account. The experimental acceptance acts to lower both N_C and N_{IMF} and produces a slight steepening of the correlation. Excellent agreement between the experimental data (solid points) and the filtered statistical calculations for expanding nuclear systems is obtained.

In summary, we have studied the $^{129}Xe + ^{197}Au$ reaction at E/A = 50 MeV with a low-threshold 4π detection system. We have characterized multifragment decays of this system as a function of the

detected charged particle multiplicity. In collisions in which more than 33 charged particles are detected, an average of six intermediate mass fragments was observed. For these collisions, intermediate mass fragments constitute 16-17% of all detected charged particles. Much too small fragment multiplicities are predicted by the Quasi-Particle Dynamics model[6]. Similarly, statistical model calculations of the decay of equilibrated nuclei at normal density[8,9] predict too few intermediate mass fragments. The observed relation between charged particle and intermediate mass fragment multiplicities can be reproduced by calculations of the decay of an expanding nuclear system[11] characterized by a soft equation of state at low density.

a. Present address: Instituto de Fisica, Universidade de Sao Paulo, C. Postal 20516, CEP 01498, Sao Paulo, Brazil
b. Nuclear Science Division, Lawrence Berkeley Laboratory, Berkeley, CA 94720
c. Accelerator and Fusion Research Division, Lawrence Berkeley Laboratory, Berkeley, CA 94720
d. Department of Physics, University of Wisconsin, Madison, WI 53706

References

1. W. Lynch, Ann. Rev. Nucl. Part. Sci., 37, 493 (1987).
2. D.H.E. Gross, Rep. Prog. Phys. 53, 605 (1990).
3. R.T. de Souza et al., Nucl. Instr. and Meth. A295, 109 (1990).
4. W.L. Kehoe et al., Nucl. Instr. and Meth. A311, 258 (1992).
5. Double-hit alpha particles are cleanly separated from Li fragments with the Miniball. If Li fragments are excluded, the average IMF multiplicity for $N_C \geq 33$ is reduced to $\langle N_{IMF} \rangle = 4.7$.
6. D.H. Boal and J.N. Glosli, Phys. Rev. C37, 91 (1988); C42, R502 (1990).
7. For central collisions, complete overlap of projectile and target occurs at $t \approx 50$ fm/c.
8. R.J. Charity et al., Nucl. Phys. A483, 371 (1988).
9. W.A. Friedman and W.G. Lynch, Phys. Rev. C28, 16 (1983); C28,950 (1983).
10. We have also performed calculations assuming different charge-to-mass ratios, Z/A = 0.367-0.433, for the decaying nuclei. The conclusions remain the same.
11. W.A. Friedman, Phys. Rev. C42, 667 (1990).
12. Even larger fragment multiplicities are predicted for non-zero collective expansion energies. For example, an initial expansion kinetic energy of 50 MeV increases the predicted IMF multiplicities by roughly one unit.

EVENT-MIXING ANALYSIS OF TWO-PROTON CORRELATION FUNCTIONS

M.A. Lisa, W.G. Gong, C.K. Gelbke, and W.G. Lynch

The technique of intensity interferometry allows the extraction of valuable information about the space-time characteristics governing the decay of hot nuclear systems [1-13]. Two-particle correlation functions offer a convenient way of presenting such information. Most theoretical treatments are based upon the assumption that the final-state interaction between the two detected particles dominate, that final-state interactions with all remaining particles can be neglected, and that the correlation functions are determined by the two-body density of states as corrected by the interactions between the two particles. Hence, the theoretical expression for the correlation function is the ratio of available states with and without interaction between the particle pair. This ratio depends on the spatial dimensions of the region of phase space occupied by the emitted particles [1,2,3,6,7,11].

For collisions at fixed impact parameter, the correlation function $1+R(\vec{P},\vec{q})$ is related to the single- and two-particle yields, $Y(\vec{p})$ and $Y(\vec{p}_1,\vec{p}_2)=Y(\vec{P},\vec{q})$:

$$Y(\vec{P},\vec{q}) = Y(\vec{p}_1,\vec{p}_2) = C(1+R(\vec{P},\vec{q}))\,Y(\vec{p}_1)Y(\vec{p}_2) \ , \qquad (1)$$

where $\vec{p}_1$ and $\vec{p}_2$ denote the momenta of the two detected particles, $\vec{P}=\vec{p}_1+\vec{p}_2$ is the total momentum of the particle pair, and $\vec{q}$ is the momentum of relative motion (defined in the center-of-momentum frame of the particle pair, where $\vec{P}=0$; non-relativistically, $\vec{q}=\mu\vec{v}_{rel}$). The constant C can be determined from the condition that $R(\vec{P},\vec{q})=0$ for sufficiently large relative momenta for which modifications of the two-particle phase-space density due to quantum statistics or final-state interactions become negligible.

Since the impact parameter of a subatomic collision cannot be measured with precision, experimental determinations of two-particle correlation functions involve averages over impact parameter. Furthermore, it is virtually impossible to collect sufficient statistics to allow the determination the full six-dimensional dependence of correlation function upon $\vec{P}$ and $\vec{q}$. Hence, implicit integrations are carried out in the construction of experimental correlation functions. For example, experimental correlation functions are mostly defined according to the relation [1]:

$$\Sigma\, Y(\vec{p}_1,\vec{p}_2) = C^{\dagger}(1+R(\zeta)) \bullet \Sigma\, Y^{\dagger}(\vec{p}_1,\vec{p}_2) \ . \qquad (2)$$

In Eq. 2, $Y^{\dagger}(p_1,p_2)$ is the "background" yield, $C^{\dagger}$ is a normalization constant which ensures proper normalization at large relative momenta, and ζ is the variable for which the explicit dependence of the correlation function is evaluated (the most common choice is $\zeta=q$). For each experimental gating condition (representing implicit integrations over a number of variables), the sums on both sides of Eq. 2 are extended over all energy and detector combinations corresponding to the given bins of ζ. The experimental correlation function is defined in terms of the ratio of these two sums. Comparisons with theoretical results must take this definition into account, see also the discussion given in the appendix of ref. [12].

Two different approaches are commonly used for the construction of the background yield. In one approach (referred to as the "singles technique"), the background yield is taken as proportional to the product of the single particle yields, measured with the same external trigger conditions as the true two-particle coincidence yield [4,9,10,12,13]:

$$Y^{\dagger}(\vec{p}_1,\vec{p}_2) \propto Y(\vec{p}_1)Y(\vec{p}_2) \ . \qquad (3)$$

In the other approach (referred to as the "event-mixing technique"), the background yield is generated by mixing particle yields from different coincidence events [2,5,8]:

$$Y^{\dagger}(\vec{p}_1,\vec{p}_2) = \sum_{n\neq m} \delta^3(\vec{p}_1-p_{1,n})\delta^3(\vec{p}_2-p_{2,m}) \ . \qquad (4)$$

Here, the indices n and m label the n-th and m-th recorded two-particle coincidence events, and $p_{1,n}$ and $p_{2,m}$ denote the momenta of particles 1 and 2 recorded in events n and m, respectively. In most analyses, the index n runs over all recorded coincidence events and the index m is varied according to m=n+k, with typically $0<k<1000$.

The main advantage of the event-mixing technique is its simplicity, as no singles measurements are necessary. In some situations, single- and two-particle data could represent different averages of impact parameter. In such cases, the use of the singles technique could lead to serious distortions of the correlation function [8] which could complicate comparisons with theoretical predictions. Furthermore, less interesting correlations, resulting for example from phase space constraints due to conservation laws [4], may be suppressed by using the event-mixing technique. However, the event-mixing technique also attenuates the very correlations one wishes to measure [5]. The degree of attenuation depends on the phase space acceptance of the experimental apparatus and on the magnitude

of the correlations. Quantitative analyses require careful Monte-Carlo simulations. For the extraction of undistorted correlation functions iterative procedures have been developed [5].

For statistical emission processes in which the emission of a single particle has negligible effect on further emissions, single and two-particle yields should originate from similar regions of impact parameters. In such instances, the singles technique appears to be the preferential choice since it avoids the attenuation of the very correlations one wishes to measure. There are, however, scenarios where the singles technique may become inappropriate. For example, emission to extreme forward angles may have large contributions from breakup reactions in which only one particle is emitted [8]. In such instances, single and two-particle detection will select different classes of collisions.

Two-proton correlations generated with the singles technique display a strong dependence on the total energy (or momentum) of the emitted particle pairs [4,9,10,12]. In a recent paper [8], the issue was raised that this dependence might be an artifact of the singles technique employed for the construction of the experimental correlation function. In this paper we address this question and give a quantitative comparison of two-proton correlation functions constructed by the two techniques. For this purpose, we have re-analyzed the high-statistics data of ref. [10,12] taken for the $^{14}N+^{27}Al$ reaction at E/A=75 MeV.

In our event-mixing analysis, we have first projected out "pseudo-singles" spectra from the two-proton yields:

$$Y^{*}(\vec{p}) = \sum_{i,\,n} \delta^{3}(\vec{p}-\vec{p}_{i,n}) \,, \qquad (5)$$

where $\vec{p}_{i,n}$ is the momentum of the i-th proton (i=1,2) detected in the n-th two-proton coincidence event. These pseudo-singles yields were then inserted into Eq. 3 to generate the background yield. This procedure is equivalent to summing Eq. 4 over all event indices n and (n+m), thus also allowing a contamination of contributions from true coincidences (m=0). In our analysis, this contamination is entirely negligible ($<10^{-6}$). The background constructed via Eqs. 3 and 5 provides the maximum statistical accuracy which can be obtained with the event-mixing technique.

Useful insight can be gleaned by comparing true singles and pseudo-singles yields. In Fig. 1, energy spectra are compared for three representative regions of angle covered by the experimental apparatus of ref. [10,12]. In Fig. 2, angular distributions are compared for three different energy intervals. Clearly singles and pseudo-singles yields are very similar.

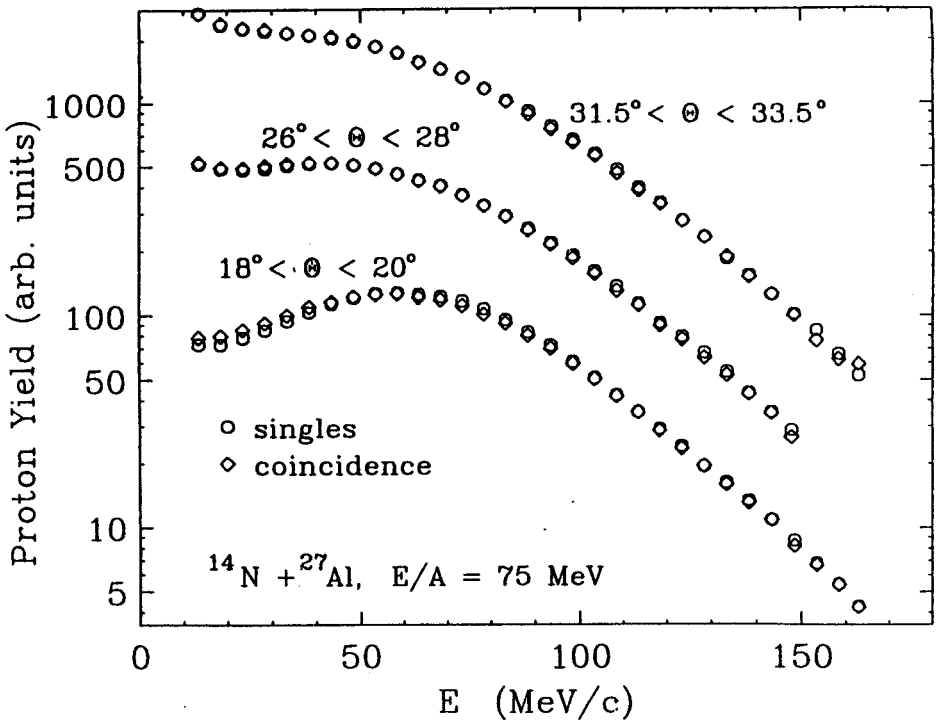

Figure 1: Comparison of singles (circles) and pseudo-singles (diamonds) energy spectra measured [30,32] for the $^{14}N+^{27}Al$ preaction at E/A=75 MeV. (Statistical errors are smaller than the size of the symbols.)

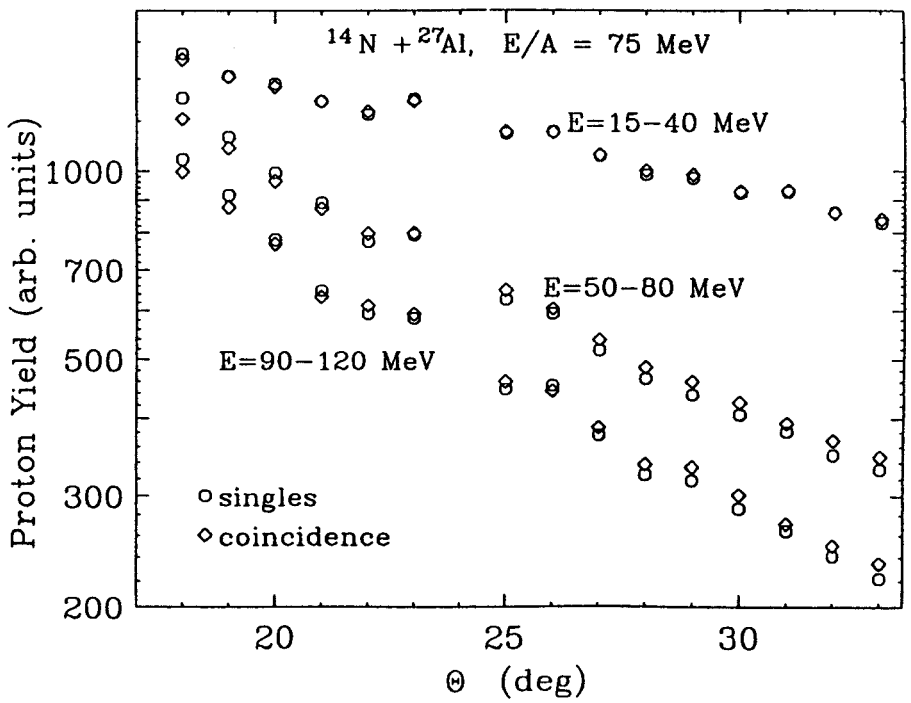

Figure 2: Comparisons of singles (circles) and pseudo-singles (diamonds) angular distributions measured [10,12] for the $^{14}N+^{27}Al$ reaction at E/A=75 MeV. (Statistical errors are smaller than the size of the symbols.)

Figure 3 gives a comparison of two-proton correlation functions constructed with the two techniques, using the same momentum gates as displayed in Fig. 14 of ref. [12]. Very similar results are obtained by the two techniques. In particular, both techniques give very similar momentum dependences of the two-proton correlation functions. As expected, the event-mixing technique gives correlation functions which are slightly attenuated in comparison with the singles technique. The differences are small (typically smaller than 5%) and only of marginal statistical significance.

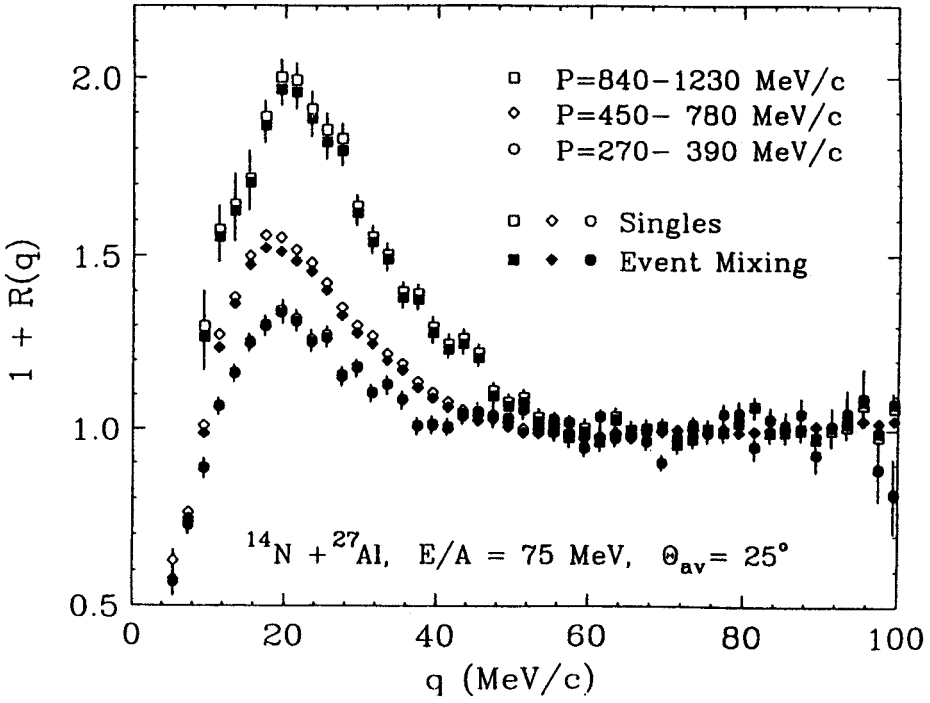

Figure 3: Two-proton correlation functions measured [10,12] for the ^{14}N+^{27}Al reaction at E/A=75 MeV. Open and solid points represent correlation functions constructed by the singles and event-mixing techniques, respectively. Momentum cuts are indicated in the figure. Statistical errors (larger than the size of the data points) are only shown for open points, solid points have errors of same magnitude.

We also explored whether the results were stable with respect to the number of detectors employed in the experiment. In Fig. 4, we show energy-integrated two-proton correlation functions from data in which the entire hodoscope (top panel), only 23 detectors (center panel) and only 7 detectors were incorporated into the analysis. (Integration over all outgoing particle energies was performed to ensure good statistical accuracy for the analysis employing only 7 detectors.) Again, the two techniques give rather similar results. Here again, however, correlation functions obtained with the event-mixing technique are slightly attenuated as compared to those constructed with the singles

technique reflecting the presence of correlations in the background yields constructed from event-mixing analyses [5].

In conclusion, the momentum (or energy) dependence of two-proton correlation functions reported in ref. [10,12] can be considered as firmly established. A re-analysis of the data of ref. [10,12] in terms of a background constructed by event-mixing gives correlation functions which are very similar (though slightly attenuated) to those published previously.

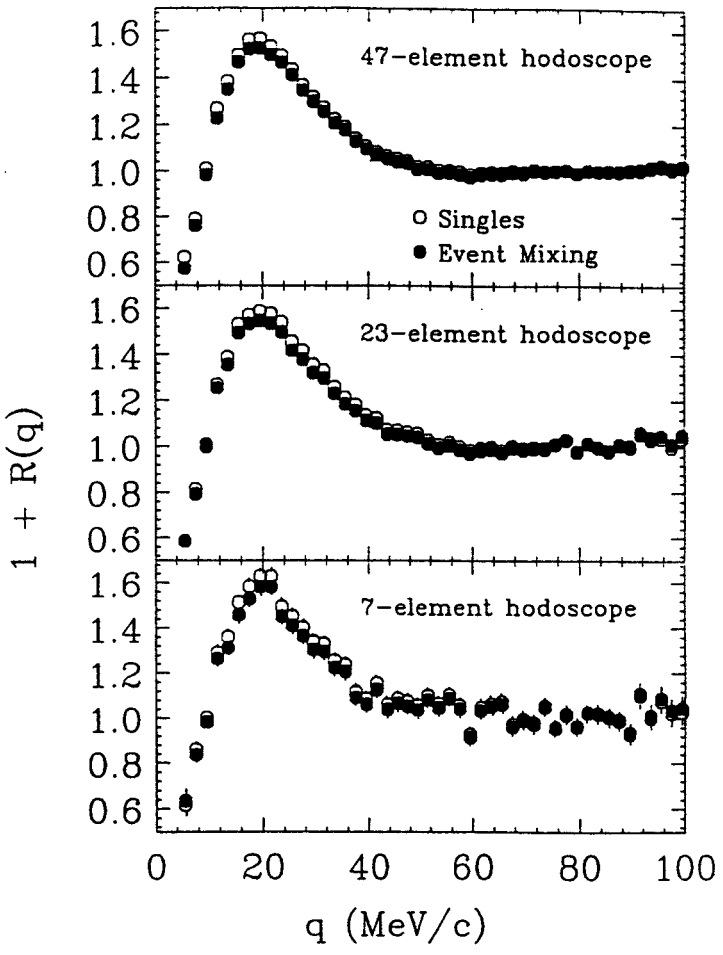

Figure 4: Energy integrated two-proton correlation functions measured [10,12] for the $^{14}N+^{27}Al$ reaction at E/A=75 MeV. Open and solid points represent correlation functions constructed by the singles and event-mixing techniques, respectively. Top, center, and bottom panels represent correlation functions extracted from arrays consisting of 47, 23, and 7 detectors, respectively. Statistical errors (larger than the size of the data points) are only shown for open points, solid points have errors of same magnitude.

References

1. For a recent review, see e.g. D.H. Boal, C.K. Gelbke, and B.K. Jennings, Rev. Mod. Phys. 62, 553 (1990).
2. G.I. Kopylov, Phys. Lett. B50, 472 (1974).
3. S.E. Koonin, Phys. Lett. 70B, 43 (1977).

4. W.G. Lynch, C.B. Chitwood, M.B. Tsang, D.J. Fields, D.R. Klesch, C.K. Gelbke, G.R. Young, T.C. Awes, R.L. Ferguson, F.E. Obenshain, F. Plasil, R.L. Robinson and A.D. Panagiotou, Phys. Rev. Lett. 51, 1850 (1983).
5. W.A. Zajc, J.A. Bisterlich, R.R. Bossingham, H.R. Bowman, C.W. Clawson, K.M. Crowe, K.A. Framkel, J.G. Ingersoll, J.M. Kurk, C.J. Martoff, D.J. Murphy, J.O> Rasmussen, J.P. Sullivan, E. Yoo, O. Hashimotot, M. Koike, W.J. McDonald, J.P> Miller, and P. Truöl, Phys. Rev. C29, 2173 (1984).
6. S. Pratt, Phys. Rev. Lett. 53, 1219 (1984).
7. S. Pratt and M.B. Tsang, Phys. Rev. C36, 2390 (1987).
8. D. Rebreyend, S. Kox, J.C. Gondrand, B. Khelfaoui, F. Merchez, B. Norén, and C. Perrin, Proceedings of the International Workshop on Particle Correlations and Interferometry in Nuclear Collisions, held at Château Clermont, Le Cellier, France, June 28-30, 1990, edited by D. Ardouin, World Scientific Publishing Co., Singapore, 1990, 93.
9. W.G. Gong, C.K. Gelbke, N. Carlin, R.T. de Souza, Y.D. Kim, W.G. Lynch, T. Murakami, G. Poggi, D. Sanderson, M.B. Tsang, H.M. Xu, D.E. Fields, K. Kwiatkowski, R. Planeta, V.E. Viola, Jr., S.J. Yennello, and S. Pratt, Phys. Lett. B246, 21 (1990).
10. W.G. Gong, W. Bauer, C.K. Gelbke, N. Carlin, R.T. de Souza, Y.D. Kim, W.G. Lynch, T. Murakami, G. Poggi, D.P. Sanderson, M.B. Tsang, H.M. Xu, S. Pratt, D.E. Fields, K. Kwiatkowski, R. Planeta, V.E. Viola, Jr., and S.J. Yennello, Phys. Rev. Lett. 65, 2114 (1990).
11. W.G. Gong, W.Bauer, C.K. Gelbke, and S. Pratt, Phys. Rev. C43, 781 (1991).
12. W.G. Gong, C.K. Gelbke, W. Bauer, N. Carlin, R.T. de Souza, Y.D. Kim, W.G. Lynch, T. Murakami, G. Poggi, D.P. Sanderson, M.B. Tsang, H.M. Xu, D.E. Fields, K. Kwiatkowski, R. Planeta, V.E. Viola, Jr., S.J. Yennello, and S. Pratt, Phys. Rev. C43, 1804 (1991).
13. Y.D. Kim, R.T. de Souza, D.R. Bowman, N. Carlin, C.K. Gelbke, W.G. Gong, W.G. Lynch, L. Phair, M.B. Tsang, F. Zhu, and S. Pratt, Phys. Rev. Lett. 67, 14 (1991).

MULTIFRAGMENT EMISSION IN THE REACTION $^{36}Ar + ^{197}Au$ AT E/A = 35, 50, 80, AND 110 MeV

R.T. de Souza[a], L. Phair, D.R. Bowman, N. Carlin[b], W.A. Friedman[c], C.K. Gelbke, W.G. Gong[d], Y.D. Kim[a], M.A. Lisa, W.G. Lynch, G.F. Peaslee, M.B. Tsang, and F. Zhu

Under extreme conditions of temperature and pressure, nuclear matter may preferentially decay by multifragment emission[1-6]. Such a decay mode would represent a new and interesting phenomenon. Many mechanisms have been proposed[1-14] for the production of the fragments. For example, the action of thermal pressure may force hot, nuclear systems to expand to low density where the exponential growth of density fluctuations may lead to a complete disintegration of the nuclear system[1,4]. Unfortunately, detailed comparisons of various fragment production models to experimental data have been lacking since few experiments[15-20] performed to date provided sufficient phase space coverage to allow the extraction of exclusive quantities. To address this question of multifragment decay of highly excited nuclear systems and to provide constraints for various theoretical models, we have measured both total charged particle and intermediate mass fragment (IMF: $3 \le Z \le 20$) multiplicities for the $^{36}Ar + ^{197}Au$ reaction at E/A = 35, 50, 80, and 110 MeV.

The experiment was performed by bombarding a 1 mg/cm^2 ^{197}Au target with ^{36}Ar beams of E/A = 35, 50, 80, and 110 MeV accelerated by the K1200 cyclotron . Reaction products of a nuclear collision were detected with the Miniball[21], a low-threshold 4π detector array covering polar angles of $9° \le \theta \le 160°$ with a geometric efficiency of 89% of 4π. The measurements at E/A=35 MeV were performed with reduced angular coverage, $16° \le \theta \le 160°$. Quasi-elastic projectile-like fragments as well as heavy residues emitted at more forward angles were not detected. Reaction products were identified by atomic number for Z=1-20 with representative detection thresholds of E/A=2, 3, and 4 MeV for Z=3, 10, and 18 fragments, respectively.

For a given event, we define the charged particle multiplicity N_C as the number of detectors in which at least one charged particle is recorded, including low energy fragments stopped in the plastic scintillator foils. Consistent with the definition adopted in ref. 27, IMF multiplicities presented in this report do not include unidentified low energy fragments which were stopped in the plastic scintillator foils. As a result, the IMF multiplicities for the $^{36}Ar+^{197}Au$ reaction are slightly lower than those reported in ref. 26.

To characterize the various classes of multifragment events, we have extracted the probability distributions $P(N_{IMF})$ of detecting N_{IMF} intermediate mass fragments in a single collision for different gates on the charged particle multiplicity N_C. The four panels in Fig. 1 depict these distributions. At each energy, the IMF multiplicity distributions become wider and shift towards higher average multiplicities as the charged particle multiplicity increases.

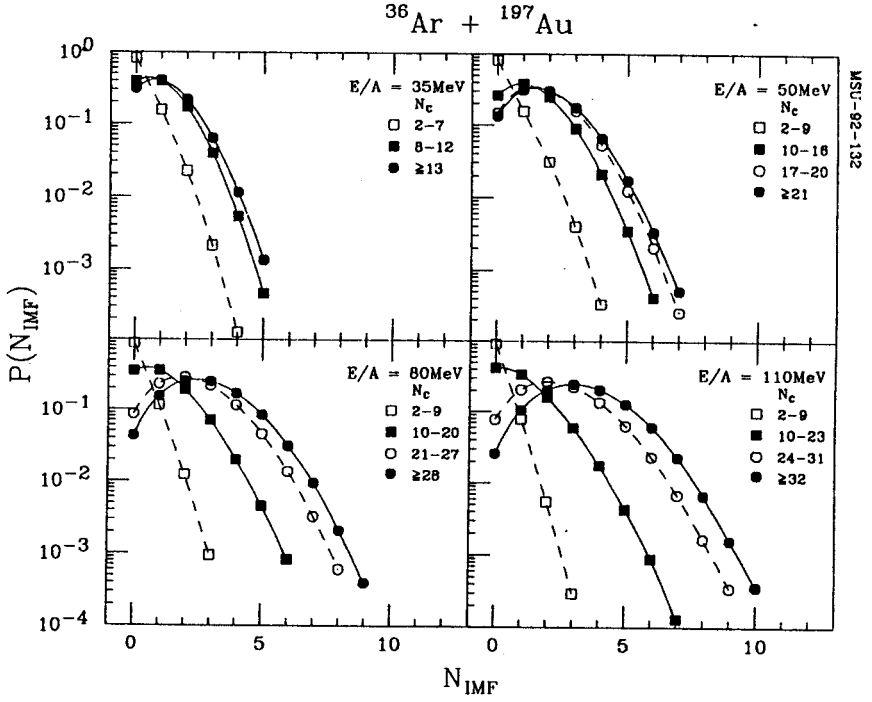

Figure 1: Measured IMF multiplicity distributions for the indicated gates on charged particle multiplicity N_C. Panels are labeled by incident energy.

Peripheral reactions, selected by $N_C \leq 7$, exhibit narrow IMF multiplicity distributions peaked at $N_{IMF}=0$. For these collisions, IMF emission is an unlikely process. On the other hand, for central collisions,selected by large values of N_C, IMF emission is a common process for which the average IMF multiplicity increases from $\langle N_{IMF} \rangle \cong 1$ at E/A=35 MeV to $\langle N_{IMF} \rangle \cong 4$ at E/A=110 MeV. At the highest incident energy, events are observed in which more than 10 intermediate mass fragments are detected in the exit channel.

To allow quantitative comparisons of IMF multiplicity distributions, we have determined their first and second moments, $\langle N_{IMF} \rangle$ and σ^2_{IMF}. The dependence of these moments on the total charged particle multiplicity N_C is shown in Fig. 2. Values extracted at different incident energies are shown by different symbols as indicated by the key in the figure. At all energies, $\langle N_{IMF} \rangle$ and σ^2_{IMF} exhibit an initial, approximately linear increase as a function of N_C. The slope of this increase is rather similar for the four energies investigated. For large values of N_C, corresponding to the extreme tails of the respective N_C distributions, both $\langle N_{IMF} \rangle$ and σ^2_{IMF} increase only marginally as a function of N_C.

The relationship between the IMF and total charged particle multiplicities can be qualitatively understood by assuming that the charged particle multiplicty is strongly correlated with energy deposition and that the production of intermediate mass fragments depends primarily upon this energy deposition. The nearly universal increase of $\langle N_{IMF} \rangle$ as a

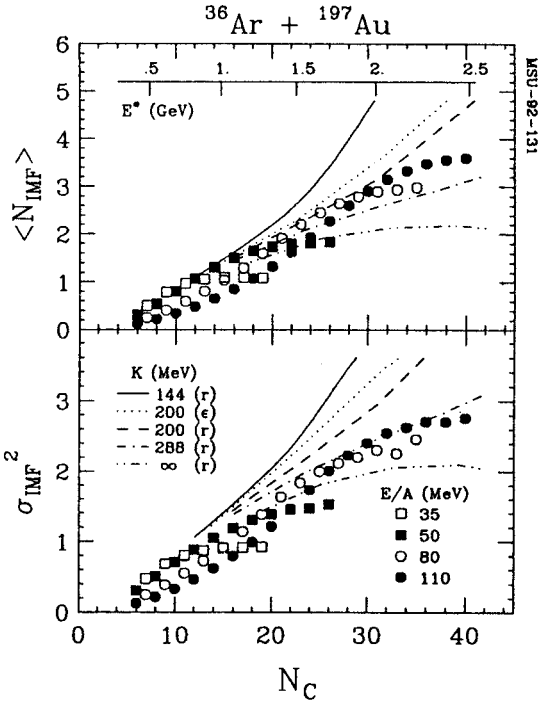

Figure 2: First and second moments of IMF multiplicity distributions as a function of charged particle multiplicity, N_C. Different symbols represent results for indicated beam energies. The solid, dashed, dotted-dashed, and dashed-dotted-dotted curves show results calculated for the statistical decay of expanding compound nuclei of finite-nucleus compressibility K=144, 200, 288, and ∞, respectively. The dotted curves represent the calculations for K=200, filtered by the detector response.

function of N_C can thus be viewed as due to the selection of interactions involving a progressively increasing amount of internal energy deposition. For orientation, the upper panel of Fig. 2 includes an approximate scale of the relation between the excitation energy of the emitting system and the mean charged particle multiplicity calculated from the statistical model of ref. 6. In the extreme tails of the N_C distributions, the correlation bewteen internal energy and N_C becomes dominated by fluctuations of the charged particle multiplicity. Hence, very large values of N_C become ineffective in selecting nuclei of increasing internal energy thus causing the observed saturation of $<N_{IMF}>$ and σ^2_{IMF} at large values of N_C.

We have compared the experimentally measured IMF multiplicity distributions with the predictions of the decay model discussed in ref. 6. This schematic model couples the phase-space features of statistical decay with the dynamical features of expansion. It has the capacity for predicting both multiplicity distributions of species of particles (IMFs in particular)and their spectra. The model has been successfully employed[22] to interpret the low emission temperatures deduced from the relative population of states[23], as well as the trends in IMF multiplicity with excitation energy[17] where the multiplicity is found and predicted to be less than one[24]. It also predicted[6] a sharp rise in multiplicity for excitation energies on the order of 8 MeV/nucleon.

The calculations require an assumption of initial source mass, charge, and thermal excitation energy when the system is at normal density. For simplicity we assumed the decaying source to be the full composite system (A=233, Z=97), and we further assumed that the system expanded with no initial expansion velocity from normal density. While varying the excitation energy we noted the correlation between the predicted total charged particle multiplicity and the features of the predicted IMF multiplicity distributions. The model ignores angular momentum, fluctuations in source size and excitation energy, and the lack of thermal equilibrium. While the inclusion of such effects might affect the final observations, we nonetheless find that the essential features of the observed data are included in the predictions of the schematic model shown by the curves in Fig. 2. The sensitivity to the source size was explored by changing the initial mass and charge by 20%. The qualitative conclusions remain valid despite this change.

The calculations are sensitive to the assumption of nuclear compressibility at low density. The solid, dashed, and dashed-dotted curves in Fig. 2 show predictions for the relationship between the mean IMF and charged particle multiplicities for finite-nucleus compressibilities of K=144, 200, and 288 MeV, respectively[25]. IMF multiplicities for a non-expanding compound nucleus, corresponding to the limit $K\rightarrow\infty$, are shown by the dashed-dotted-dotted curves. To illustrate instrumental distortions, the dotted curves show the calculations for K=200 MeV, filtered by the response of the experimental apparatus; such distortions are too small to affect the qualitative conclusions of this paper. At low multiplicities, corresponding to low excitation in this model, the nucleus does not expand and all calculations predict IMF multiplicities consistent with the measured values. For multiplicities larger than $N_C \cong 20$, however, the expansion strongly influences the predicted number of clusters in the final state. Large observed IMF multiplicities comparable to the measured values are only predicted for an equation of state that is sufficiently soft to allow the nucleus to expand in response to thermal pressure. Very stiff low-density equations of state hinder the expansion of the system leading to a suppression of the production of multifragment final states.

The calculations with the schematic model suggest that multifragment decays of highly excited nuclear systems may exhibit considerable sensitivity to the low-density nuclear equation of state. They indicate that the expansion dynamics, which is governed by this property, may be intimately connected to the production of IMFs. A more quantitative exploration of these properties, however, will require a more complete model.

We have also performed calculations with the microscopic quasi-particle dynamics (QPD) model of ref. 11. In collisions leading to a total multiplicity of 36-45, these calculations predict average multiplicities of significantly less than one for fragments with $3 \leq Z \leq 20$ and, in addition, the formation of a single heavy residue. These predicted IMF multiplicities are much smaller than those observed experimentally.

In summary, we have studied multifragment emission in $^{36}Ar+^{197}Au$ reactions over a broad range of incident energies. The mean values and variances of the multiplicity distributions of intermediate mass fragments were found to increase as a function of the total charged particle multiplicity which may be interpreted as a rough measure for the internal energy of the fragment emitting system. An average multiplicity of 4 intermediate mass fragments is observed for the most central collisions at E/A=110 MeV. These large IMF multiplicities are consistent with predictions of a statistical model for evaporation from an expanding compound nucleus. Calculations with the quasi-particle dynamics model of ref. 11 predict too low fragment multiplicities.

a. Indiana University Cyclotron Facility, Indiana Univ. Bloomington, IN 47405, USA
b. Instituto de Fisica, Universidade de Sao Paulo, Brazil
c. Department of Physics, University of Wisconsin, Madison, WI 53706, USA
d. Lawrence Berkeley Laboratory, Berkeley, CA 94720, USA

References

1. G. Bertsch and P.J. Siemens, Phys. Lett. **126B** (1983) 9.
2. L.P. Cernai and J. Kapusta, Phys. Reports **131** (1986) 223.
3. W. Lynch, Ann. Rev. Nucl. Part. Sci. **37** (1987) 493, and refs. therein.
4. T.J. Schlagel and V.R. Pandharipande, Phys. Rev. **C36** (1987) 162.
5. D.H.E. Gross, Rep. Prog. Phys. **53** (1990) 605, and refs. therein.
6. W.A. Friedman, Phys. Rev. **C42** (1990) 667.
7. L.G. Moretto, Nucl. Phys. **A247** (1975) 211.
8. W.A. Friedman and W.G. Lynch, Phys. Rev. **C28** (1983) 16; **C28** (1983) 950.
9. W. Bauer et al., Phys. Rev. Lett. **58** (1987) 863.
10. G. Peilert et al., Phys. Rev. **C39** (1989) 1402.
11. D.H. Boal and J.N. Glosli, Phys. Rev. **C37** (1988) 91; **C42** (1990) R502.
12. W. Bauer et al., Phys. Lett. **B150** (1985) 53, Nucl. Phys. **A452** (986) 699.
13. T.S. Biro et al., Nucl. Phys. **A459** (1986) 692.
14. C. Cerruti et al., Nucl. Phys. **A476** (1988) 74.
15. K.G.R. Doss et al., Phys. Rev. Lett. **59** (1987) 2720.
16. R. Bougault et al., Nucl. Phys. **A488** (1988) 255c.
17. R. Trockel et al., Phys. Rev. **C39** (1989) 729.
18. R. Bougault et al., Phys. Lett. **B232** (1989) 291.
19. Y.D. Kim et al., Phys. Rev. Lett. **63** (1989) 494.
20. Y. Blumenfeld et al., Phys. Rev. Lett. **66** (1991) 576.
21. R.T. de Souza et al. Nucl. Instr. and Meth. **A295** (1990) 109.
22. W.A. Friedman, Phys. Rev. Lett. **60** (1988) 2125.
23. Z. Chen et al., Phys. Rev. **C36** (1987) 2297, and refs. therein.
24. W.A. Friedman, Phys. Rev. **C40** (1989) 2055.
25. J.P. Blaizot, Phys. Reports **64** (1980) 171.
26. R.T. de Souza et al., Phys. Lett. **B268** (1991) 6.
27. D.R. Bowman et al., Phys. Rev. Lett. **67** (1991) 1527.

MULTIFRAGMENT EMISSION IN $^{36}Ar+^{197}Au$ AND $^{129}Xe+^{197}Au$ COLLISIONS: PERCOLATION MODEL

L. Phair, W. Bauer, D.R. Bowman, N. Carlin[a], N. Colonna[b], R.T. de Souza[c], C.K. Gelbke, W.G. Gong[b],K. Hanold[b], Y.D. Kim[c], M.A. Lisa, W.G. Lynch, M.A. McMahan[b],L.G. Moretto[b], G.F. Peaslee, M.B. Tsang, C. Williams, G.J. Wozniak[b], and F. Zhu

Multifragment disintegrations of highly excited nuclear systems might carry information about the equation of state and the liquid gas phase transition of low density nuclear matter (refs. 1-6 and references given therein). In rather general terms,[1,3] the fluctuations at the critical point of the nuclear matter phase diagram are expected to lead to mass distributions which follow a power law, $\sigma(A)\sim A^{-\tau}$ with a critical exponent of the order of τ=2.2-2.3. A number of theoretical investigations of phase transitions in finite nuclear systems have been based on percolation models[7-14]. Percolation models are attractive, since they exhibit a well-defined phase transition for infinite systems and since they allow straightforward generalizations to finite systems and the incorporation of important geometrical ingredients[13] for multifragmenting systems. Percolation models have also been useful for the development of techniques to extract critical exponents from exclusive fragmentation data[11,12]. Most percolation models are, however, governed by a single bond-breaking or site-vacancy parameter and cannot be expected to reproduce the two-dimensional phase diagram of nuclear matter in the temperature vs. density plane. Despite this limitation, percolation models have been rather successful[7-9] in describing the observed[3] power-law behavior of measured fragment mass distributions and in developing techniques to extract critical exponents. In this letter, we provide a test of the bond-percolation model of refs. 7-9 and compare its predictions to fragment yields measured with a low-threshold 4π, detector for the reactions $^{129}Xe+^{197}Au$ at E/A=50 MeV and $^{36}Ar+^{197}Au$ at E/A=50, 80, 110 MeV.

The experiments were performed with beams from the K1200 cyclotron. Reaction products were detected with the Miniball phoswich detector array[15]. Each phoswich detector consisted of a 40 μm thick plastic scintillator foil backed by a 2 cm thick CsI(Tl) crystal. (For detectors in Ring 1, the scintillator foil was 50 μm thick.) For the $^{129}Xe+^{197}Au$ reaction, the most forward angles were covered by a 16-element hodoscope, each element of which consisted of two position-sensitive solid-state detectors (300 μm and 5 mm thick) and a 7.6 cm thick plastic scintillator[16]. Fragments detected in the Miniball were identified by element for Z=1-20; representative detection thresholds were 2, 3, and 4 MeV/nucleon for Z=3, 10, and 18 fragments, respectively. Fragments detected in the forward array were identified by element for Z=1-54; representative detection thresholds were 6, 13, 21, and 27 MeV/nucleon for Z=2, 8, 20, and 54

fragments, respectively. Additional technical details and details of the detector geometries can be found in refs. 15-18.

Calculations were performed with the bond percolation model of ref. 7-9. In this model, the nucleus is considered to be a cubic lattice, the sites of which are randomly occupied by protons and neutrons. Initially, all nucleons are connected in one cluster. The bonds between the sites are randomly broken with a probability p. Each nucleon is assigned a random momentum consistent with the momentum distribution of a Fermi-gas of temperature T estimated[9] from the bond-breaking probability as $T=11.7\sqrt{p}$ MeV. Emitted fragments are defined in terms of connected clusters. Initial fragment energies are calculated from the total momenta of the clusters. Final kinetic energies are calculated by incorporating the final state Coulomb repulsion between the fragments. For this purpose a given fragment partition is translated into a spatial distribution of clusters characterized by an average freeze-out density $\rho=0.2\rho_0$, where $\rho_0=0.17$ fm^{-3} is the density of normal nuclear matter. (Different choices of the freeze out density lead to slightly different shapes of the low energy portion of the energy spectrum due to changes in the Coulomb repulsion between the fragments. Such changes are of minor importance for the present investigation.) The final momenta of the emitted fragments are boosted by the velocity of the center-of-mass of projectile and target. In order to allow meaningful comparisons with our data, we have filtered the theoretical distributions with the response of the experimental apparatus.

Elemental multiplicity distributions measured for the reactions $^{36}Ar+^{197}Au$ and $^{129}Xe+^{197}Au$ are shown (as points) in the top and bottom panels of figure 1. These distributions were obtained by integrating all identified fragments over all detectors. In order to select central collisions, these Z-distributions were gated by the total charged particle multiplicity cuts indicated in the figure. These cuts were chosen to represent the range of impact parameters of $b/b_{max}\leq 0.3$ when one adopts a strictly geometric interpretation of the measured charged particle multiplicity[19]. The elemental distributions observed for the various reactions exhibit rather similar shapes. For the $^{36}Ar+^{197}Au$ system (top panel), the elemental multiplicity distributions become slightly steeper with increasing bombarding energy. The multiplicities for heavier IMFs are significantly larger for the $^{129}Xe+^{197}Au$ system (bottom panel) than for the $^{36}Ar+^{197}Au$ system (top panel). Part of this difference in the observed yields of heavier fragments may be due to an increased detection efficiency in $^{129}Xe+^{197}Au$ reactions resulting from the larger center-of-mass velocity.

The curves in figure 1 depict elemental multiplicities predicted by the bond percolation model of refs. 7-9 and filtered by the detection efficiency of the experimental apparatus. Calculations are shown for representative bond-breaking probabilities above and below the critical bond breaking parameter of p=0.7. (In the percolation model, the critical point marks a

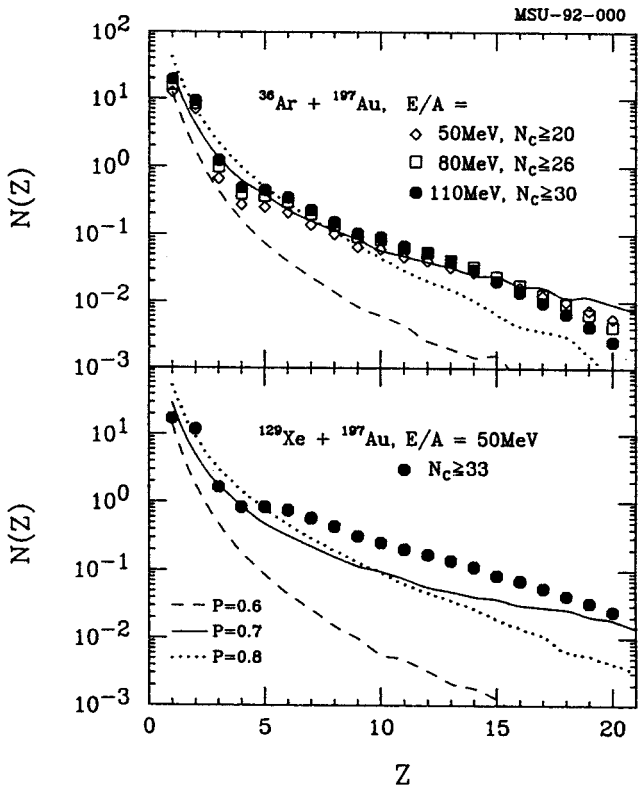

Figure 1: Elemental multiplicity distributions detected in $^{36}Ar+^{197}Au$ collisions at E/A=50, 80, 110 MeV (top panel) and in $^{129}Xe+^{197}Au$ collisions at E/A=50 MeV(bottom panel). The curves represent calculations with the bond percolation model of refs. 7-9 for the indicated bond-breaking probabilities p. The calculations are filtered by the response of the experimental apparatus.

second order phase transition; for p>0.7, the percolation cluster disappears and the system breaks up completely.) Calculations performed for bond-breaking probabilities much larger or smaller than the critical value predict Z-distributions which are too steep. For the $^{36}Ar+^{197}Au$ reactions, the overall magnitudes and shapes of the experimental Z-distributions are in reasonable agreement with predictions of the percolation model when the bond breaking parameter is taken close to the critical value. However, for the $^{129}Xe+^{197}Au$ reaction, the percolation model underpredicts the yield of heavier fragments (Z=6-20) for any choice of the bond breaking parameter.

Representative angular distributions of emitted particles are shown in figure 2. The top and bottom panels show results for the $^{36}Ar+^{197}Au$ reaction at E/A=110 MeV and for the $^{129}Xe+^{197}Au$ reaction at E/A=50 MeV, respectively. The angular distributions are shown for three different ranges of element numbers, Z=1-2 (circles), Z=3-5 (squares), and Z=6-12 (diamonds). For both systems, the angular distributions become more forward peaked with increasing fragment charge. Angular distributions for the $^{129}Xe+^{197}Au$ system are more forward peaked than those for the $^{36}Ar+^{197}Au$ system. These effects are largely due to kinematics. Differences between the angular distributions of the two reactions arise primarily from the larger velocity of the emitting source of the $^{129}Xe+^{197}Au$ system.

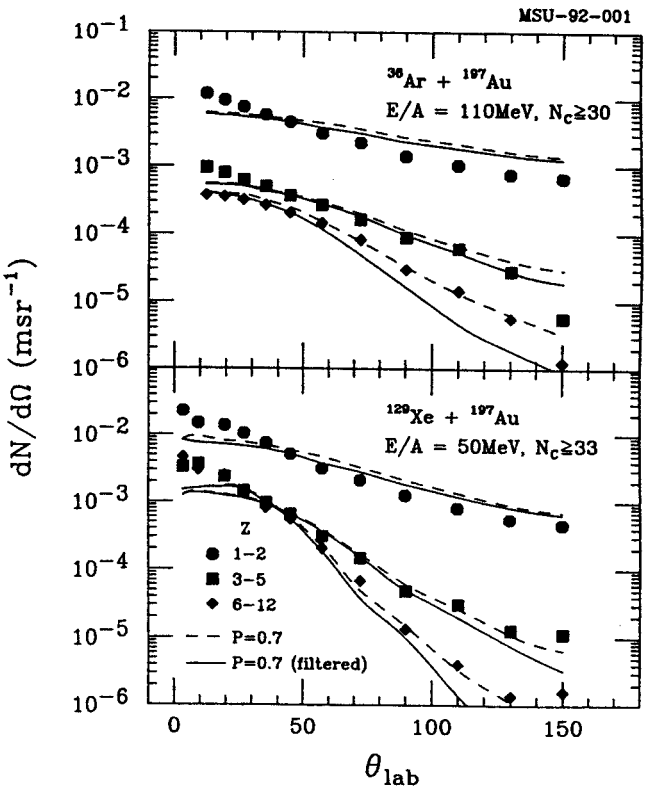

Figure 2: Angular multiplicity distributions of light particles (Z=1,2: circles), and intermediate mass fragments of Z=3-5 (squares) and Z=6-12 (diamonds) detected in ^{36}Ar+^{197}Au collisions at E/A=50, 80, 110 MeV (top panel) and in ^{129}Xe+^{197}Au collisions at E/A=50 MeV (bottom panel). The curves represent calculations with the bond percolation model of refs. 7-9 for a bond-breaking probability of p=0.7. The calculations have been normalized to the data at θ=45°. Dashed and solid curves show raw calculations and calculations filtered by the response of the experimental apparatus.

The curves in figure 2 show results of percolation calculations. To facilitate a better comparison of shapes between observed and predicted angular distributions, the calculated angular distributions were normalized to the experimental yields at θ=45°. To display the effects of the detector response, filtered and unfiltered calculations are shown by solid and dashed curves, respectively. In view of the fact that the percolation model does not include dynamical preequilibrium effects, the shapes of the experimental angular distributions are reasonably well reproduced by the calculations. Discrepancies between theoretical and experimental angular distributions due to preequilibrium emission are most pronounced for lighter fragments. For such fragments the measured angular distributions are slightly more forward peaked in the laboratory than the calculated angular distributions. Nevertheless, the angular distributions are sufficiently realistic to allow the assessment of instrumental distortions for the energy and angle-integrated particle distributions presented in figures 1 and 3.

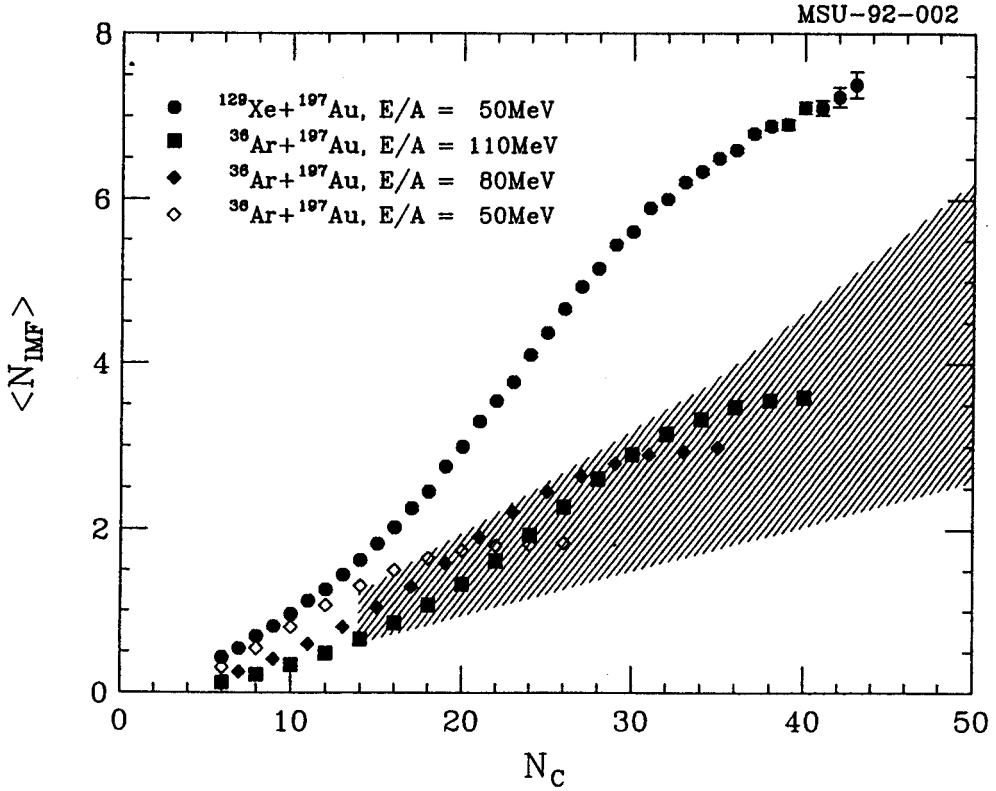

Figure 3: Relation between average IMF and charged particle multiplicities detected in ^{36}Ar+^{197}Au collisions at E/A=50, 80, 110 MeV (open diamonds, solid diamonds, squares respectively) and in ^{129}Xe+^{197}Au collisions at E/A=50 MeV (solid circles). The hatched area depicts the range of values covered by the bond-percolation model with bond breaking parameters p=0.6-0.8; the model predictions were filtered by the response of the experimental apparatus.

In order to display more clearly the fraction of IMFs among the emitted charged particles, figure 3 presents the average IMF multiplicity, $\langle N_{IMF} \rangle$, as a function of charged particle multiplicity, N_C[17,18]. For a given charged particle multiplicity, more intermediate mass fragments are observed for the ^{129}Xe+^{197}Au reaction that for the ^{36}Ar+^{197}Au reactions. According to figure 1, the percolation model underpredicts the yield of IMFs with Z>5 for the ^{129}Xe+^{197}Au reaction. This failure is displayed more clearly in figure 3 where we have evaluated the range of admixtures of IMFs among the emitted charged particles predicted by the percolation model for composite systems formed in ^{36}Ar+^{197}Au and ^{129}Xe+^{197}Au collisions. The shaded area represents the range of IMF admixtures calculated for bond-breaking parameters p=0.6-0.8. This range of bond-breaking parameters includes Z-distributions which are in rough agreement with our data (see figure 1). Larger or smaller values of the bond-breaking parameter predict too steep charge distributions and, hence, lower IMF admixtures. For the lighter ^{36}Ar+^{197}Au system, the observed ratio $\langle N_{IMF} \rangle / N_C$ lies within the range of the percolation model predictions. However, for the heavier ^{129}Xe+^{197}Au system, maximum IMF admixtures compatible with the percolation model are smaller than the experimental values by nearly a factor of two.

High resolution coincidence experiments indicate that a significant portion of primary fragments can be expected to be produced in highly excited, particle unbound states which decay by light particle emission[20]. Such sequential decay processes will result in secondary fragment yields which are smaller and secondary light particle yields which are larger than the corresponding primary yields. The portion of primary fragments may therefore be even larger than the portion of particle-stable secondary fragments. This aggravates the failure of the percolation model to predict the large proportion of intermediate mass fragments among the particles emitted in the $^{129}Xe+^{197}Au$ reaction.

The inability of the bond-percolation model to reproduce the large intermediate mass fragment multiplicities observed for the $^{129}Xe+^{197}Au$ system is unexpected and represents, to our knowledge, the first significant failure of the percolation model. This model is only one representation of a large number of phase transition models, which all belong to the same universality class and should therefore show similar deficiencies. At present it is not clear whether one can rule out all such models or whether one may be forced to consider dynamical enhancements of fragment yields due to collective expansion or rotation.

a. Instituto de Fisica, Universidade de Sao Paulo, Brazil

b. Lawrence Berkeley Laboratory, Berkeley, CA 94720, USA

c. Indiana University Cyclotron Facility, Indiana Univ. Bloomington, IN 47405, USA

References

1. P.J. Siemens, Nature **305** (1983) 410.
2. G. Bertsch and P.J. Siemens, Phys. Lett. **126B** (1983) 9.
3. A.S. Hirsch et al., Phys. Rev. **C29** (1984) 508.
4. L.P. Cernai and J. Kapusta, Phys. Reports **131** (1986) 223.
5. W.G. Lynch, Ann. Rev. Nucl. Sci. **37** (1987) 493.
6. D.H.E. Gross, Rep. Prog. Phys. **53** (1990) 605.
7. W. Bauer, D.R. Dean, U. Mosel, and U. Post, Phys. Lett. **150B** (1985) 53.
8. W. Bauer, U. Post, D.R. Dean, and U. Mosel, Nucl. Phys. **A452** (1986) 699.
9. W. Bauer, Phys. Rev. **C38** (1988) 1927.
10. X. Campi, J. Phys. **A19** (1986) L917.
11. X. Campi, Phys. Lett. **208B** (1988) 351.
12. H. NgO et al., Phys. **A337** (1990) 81.
13. T.S. Biro, J. Knoll, and J. Richert, Nucl. Phys. **A459** (1986) 692.
14. H.R. Jaqaman, G. Papp, and D.H.E. Gross, Nucl. Phys. **A514** (1990) 327.
15. R.T. de Souza et al., Nucl. Instr. and Meth. **A295** (1990) 109.
16. W.L. Kehoe et al., Lawrence Berkeley Laboratory preprint # LBL-31005.
17. R.T. de Souza et al., Phys. Lett. **B268** (1991) 6.
18. D.R. Bowman et al., Phys. Rev. Lett. **67** (1991) 1527.
19. C. Cavata et al., Phys. Rev. **C42** (1990) 1760.
20. T.K. Nayak et al., Phys. Rev. Lett. **62** (1989) 1021, and refs. therein

e^+/e^- PAIRS IN HEAVY ION REACTIONS:APEX COLLABORATION STATUS

E.Kashy, S.M. Austin, J.S. Winfield, M.R. Maier, J.E. Yurkon, and the APEX Collaboration[a]

APEX (Atlas Positron Experiment) is a collaboration[a] of research groups formed to investigate the interesting and puzzling peaks in the energy spectra of positrons emitted in heavy ion collisions near the Coulomb barrier. The experiments will use the ATLAS accelerator at Argonne National Laboratory (ANL).

The collision of ions with high Z ($\approx$ 90) provides a setting for studying phenomena associated with very large and rapidly varying electromagnetic fields. Spurred by interest in the physics of these strong fields, two research groups at GSI have measured positron spectra both in singles and in coincidence with electrons. The singles spectra show a broad distribution of positrons attributed mainly to the strong and rapidly changing electromagnetic field (so-called dynamical positrons) and, in addition, one or more relatively narrow peaks ($\approx$ 80 keV FWHM) superimposed on the broad continuum. These positron peaks have been reported [1] in collisions of ions with combined atomic numbers ranging from 162 to 188.

When positrons are observed in coincidence with electrons, the spectra representing the sum of the kinetic energies of both the positron and of the coincident electron exhibit surprisingly narrow peaks with typical widths of 15 to 25 keV. A summary of the experimental status of much of this work can be found in recent papers [1,2,3] and references therein. In all cases, statistics are limited due the relatively small cross sections involved. Speculations on the origins of these narrow (nearly monoenergetic) 'sum peaks' have been discussed in detail [4]. The goal of APEX is to obtain spectra with improved statistics as well as information on the angles of emission of both the positron and electron.

A schematic view of the APEX apparatus is shown in figure 1. Positrons and electrons produced in the collision spiral in a solenoidal magnetic field. Their energies are measured in two 36-cm long, hexagonal arrays of silicon PIN junctions. Two cylinders made of 55-cm long position sensitive NaI scintillation bars are used to differentiate the positrons from the electrons by detecting the back-to-back 511 keV photons emitted when the stopped positrons undergo annihilation. They also locate the source of the photons so that the location of the positrons in the silicon array can be identified. The emission angles are obtained from the knowledge of which silicon detector is hit by the electron or positron, and by the time of flight of that lepton from the target to the detector. Accurate angle information is obtained as long as timing resolution is shorter than the cyclotron period of the spiraling lepton. The heavy ion counter

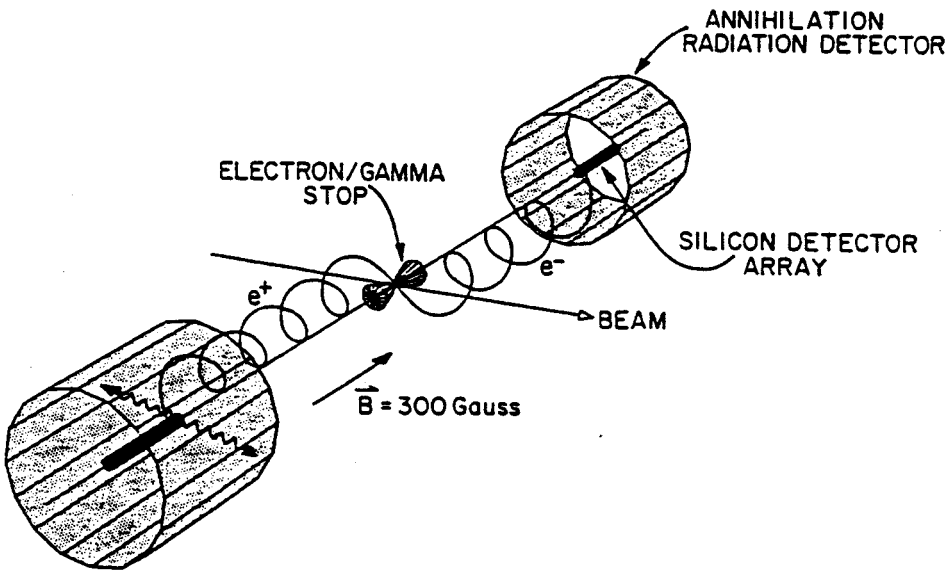

Figure 1: Schematic view of APEX apparatus. The heavy ion counter array located in the forward hemisphere is not shown.

angles from 22 to 68 degrees with respect to the incident beam.

MSU's principal contributions to APEX include the design and construction of the heavy ion counter array and gas handling system, the development of a compact low-cost preamplifier circuit and of a 16 channel Camac based constant fraction discriminator module, and the front end MASH data acquisition software [5]. MSU also provided the solenoidal magnetic field coils, which originally were part of the K-50 cyclotron.

The heavy ion counter array consists of eight trapezoidal modules, each with 3 low pressure MWPC's that use a meander delay-line readout. They provide two-dimensional position and timing information for the heavy ions involved in the reactions. A prototype was constructed and tested at MSU and met the required performance that the heavy ion emission angle can be determined with an accuracy of 0.2 degrees.

At the time of preparation of this proposal four counters have been finished. Another six are 80% complete. All will be tested with a ^{248}Am source. Isobutane at 5.3 torr and an anode voltage of 600 Volts are used. Rise times of 4 nsecs at the anode have been measured. The counters exhibit good dynamic range, with both alphas and fission fragments visible simultaneously. Differential nonlinearities appear

to be negligible.

The 16 channel constant-fraction discriminators designed at MSU for APEX are in the final testing stage at the University of Rochester, and an outside contract has been made for the production of the 55 required 16-channel units. A more detailed description of the module is in press [6]. The initial production preamplifiers have performance of resolution and timing which is acceptable though not quite as good as the prototype results obtained earlier in a test situation.

Construction of the coil mounting and of the vacuum vessel were done at PPL at Princeton University. The tank and coils are installed in the experimental hall. With a solenoidal magnetic field of 300 Gauss, the energy acceptance for positrons or electrons is from 200 to 600 keV. Procurement of the 432 required silicon detectors is almost complete, and assembly of the hexagonal arrays is proceeding at ANL. The requirements of good energy resolution ($\approx$ 6 keV) and timing ($\approx$ 2 ns) at low cost and in a restricted space put considerable demand on the detectors and on the front end electronics.

Following tests at Yale University, most of the NaI scintillator bars used to differentiate positrons from electrons have been sent to ANL. They are part of the two NaI arrays, each of which has 24 scintillators. The scintillators are used to differentiate positrons from electrons by detection of the 511 keV annihilation gammas. To minimize the ambiguity as to which Si detector has detected a positron, a goal of about 3 cm (which matches the length of the Silicon counters along the field lines) has been met for the position resolution for photons detected near the center in each of the NaI bars.

Target damage during bombardment is a well recognized problem in these experiments. Several tests of target damage have been carried out at ANL. A rotating target mechanism has been constructed at Florida State University and is in operation at ANL. Construction of high performance ion chambers to monitor the beam energy and direction as well as the target condition during bombardment has been done at the University of Washington. Development of beams for the APEX investigations at Argonne National Laboratory has begun. Beam tuning tests at target position show that beam spots of less than 2 mm diameter will be achieved.

Almost all of the electronics which were to be obtained from commercial sources has arrived. In the acquisition of data, the Si energy and timing signals will be digitized by LeCroy FERA's, and read out in zero-suppressed mode to data stacks. The presence of both energy and time signals are then checked in

ECL logic before the data is processed further.

The remarkably narrow peaks observed at GSI in complex systems involving several hundred nucleons is indeed surprising and explains the considerable effort expended in the APEX project to understand these structures.

Funding of APEX and support of some members of the collaboration is from the Department of Energy. Other participants, including MSU, are supported in part by the National Science Foundation.

a. I. Ahmad,[1] Sam M. Austin,[4] R.R. Betts,[1] F.P. Calaprice,[6] F. Chan,[8] R. Dunford,[1] J.D. Fox,[2] S. Freedman,[1] S. Gazes,[5] J.S. Greenberg,[8] A.L. Hallin,[7] T. Happ,[1] N. Kaloskamis,[8] E. Kashy,[4] C.J. Lister,[8] J. Last,[1] M.R. Maier,[4] D. Mikolas,[4] J.P. Schiffer,[1] T. Trainor,[3] P. Wilt,[1] J.S. Winfield,[4] F.L.H. Wolfs,[5] A. Wuosmaa,[1] and J.E. Yurkon[4]

[1] Argonne National Laboratory. [2] Florida State University. [3] NPL, University of Washington. [4] NSCL, Michigan State University (M.R. Maier now at L.B.L.). [5] NSRL, University of Rochester. [6] Princeton University. [7] Queen's University. [8] WNSL, Yale University.

References

1. H. Bokemeyer and W. Koenig, GSI-90-29, presented at *Xth Moriond Workshop, Les Arcs, Savoie France, Jan 20-27, 1990.*
2. W. Koenig, GSI, private communication of Corsica conference report, to be published.
3. E. Berdermann et al. GSI 90-1, p129.
4. A. Schäfer, Journal of Physics G, Nucl. Part. Phys. 15,373(1989).
5. R. Fox, R. Au, and A. Vander Molen, *IEEE Trans. Nucl. Sci.* NS-36,1608(1989).
6. M.R. Maier, M. Robertson, F.L.H. Wolfs. and P. Perera, (to be published)